Applied Thermal Engineering 289 (2026) 130000

Contents lists available at ScienceDirect

Applied Thermal Engineering

journal homepage: www.elsevier.com/locate/ate

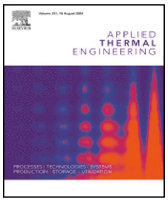

Research Paper

Experimental study of structured and unstructured roughness impact on the CHF of HFE-7100 for different saturation pressures

Ivan Talão Martins [a,b,*], Alberto Ramil Rego [b], Pablo Fariñas Alvariño [b], Luben Cabezas-Gómez [a]

[a] *Thermal and Fluid Engineering Laboratory (LETeF), Department of Mechanical Engineering, São Carlos School of Engineering (EESC), University of São Paulo (USP), Av. Trabalhador Sao-carlense, 400, São Carlos, 13561-250, São Paulo, Brazil*
[b] *Universidade da Coruña (UDC), Campus Industrial de Ferrol, Rúa Mendizábal s/n, Ferrol, 15403, A Coruña, Spain*

ARTICLE INFO

Keywords:
Nucleate pool boiling
Critical heat flux
Surface texture
Femtosecond laser

ABSTRACT

Assessment of pool boiling crisis (Critical Heat Flux - CHF - and its corresponding superheating) is of utmost importance for industrial purposes. This research pays special attention to both the temperature excursion before CHF and its corresponding uncertainty under a wide range of pressures and surface treatments. This experimental approach studies the pool boiling phenomena of saturated Novec HFE-7100 under four different pressures, namely 25, 50, 100, and 200 kPa. Six copper boiling surfaces are reported: four grinded with four different levels of sandpaper and two structured surfaces, crafted by a femtosecond laser. The roughness of the laser surfaces is within that yielded through the grinding procedure, which is interesting for comparison purposes. The yielded results show outstanding evidence: (i) The surface roughness does not modify the CHF for low pressures, which suggests the pertinence to address and determine what a plain surface is for nucleate boiling and (ii) even though both laser treatments enhance the CHF, one of the treatments yielded superheatings for CHF similar to those of the polished test section. It seems that the re-wetting mechanism promoted by the laser treatment is somehow delayed, and thus, enhances the pool boiling feasibility for a wider unexpected range of temperatures.

1. Introduction

The number of scientific documents on boiling has shown exponential growth since 1970 [2]. The wide variety of industrial applications of phase change phenomena supports this research activity. Recently published comprehensive reviews focus on procedures for heat transfer enhancement [2], fundamentals [3], critical heat flux (CHF) [4], macro/micro/nanostructured surfaces [5,6], and even the film boiling regime [7]. Previous efforts also illustrate that more fundamental knowledge is needed regarding nucleate boiling.

It is well known that experiments with boiling surfaces below a certain size cannot reproduce the behavior of an infinitely heated surface [8]. According to Lienhard and Dhir [8], the minimum size of the test section depends on the operating conditions. Note that test sections intended to work with a given fluid might not be suitable for determining the CHF for other fluids and operating conditions. This research will conduct pool boiling experiments with HFE-7100, which is a dielectric fluid from the company 3M. According to Lienhard and Dhir [8], the minimum required size for a boiling surface under the operating conditions of this research is between 24 and 30 mm for 200 and 25 kPa, respectively. The boiling surface in our test section is a circle with a diameter of 30 mm. Note that CHF determination for smaller pressures might even require larger test sections. According to Lee et al. [9], smaller boiling surfaces enhance liquid reentry and thus yield higher CHF.

Another important issue for pool boiling is the surface condition in terms of roughness. Determining when a boiling surface becomes smooth in terms of pool boiling is not straightforward. It will depend not only on the surface texture but also on the operating conditions [10]. For sufficiently low roughness values, boiling curves become almost the same [5,10], and CHF might become indistinguishable between boiling surfaces with different roughness values. It is also well known that the surface of an alloy cannot attain null roughness, if only because there are different grains in the test section. Thus, the polishing procedure cannot yield a tiny roughness even though the boiling surface is mirror-finished. Regrettably, defining when a boiling surface can be considered smooth cannot be easily addressed

---

* Corresponding author at: Universidade da Coruña (UDC), Campus Industrial de Ferrol, Rúa Mendizábal s/n, Ferrol, 15403, A Coruña, Spain.
E-mail addresses: ivan.martins@udc.es (I.T. Martins), alberto.ramil@udc.es (A.R. Rego), pablo.farinas@udc.es (P.F. Alvariño), lubencg@sc.usp.br (L. Cabezas-Gómez).

https://doi.org/10.1016/j.applthermaleng.2026.130000
Received 9 September 2025; Received in revised form 23 January 2026; Accepted 26 January 2026

Nomenclature

Acronyms

CHF	Critical Heat Flux (W m^{-2})

Roman Symbols

a, b, c	Least squares approach coefficients
C_{P_l}	Liquid specific heat at constant pressure (J $kg^{-1}K^{-1}$)
d	Diameter of the test section (m)
d_1	Distance from the nearest thermocouple of the test section to the boiling surface (m)
d_2	Distance between consecutive thermocouples of the test section (m)
h_{lg}	Latent heat of vaporization (J kg^{-1})
N_n	density of available size of cavities (active cavity sizes per m^{-2})
n	Least squares approach total discrete values (-)
P_r	Reduced pressure
$\dot{q}''$	Heat flux (W m^{-2})
R_l	Gas constant (J $kg^{-1}K^{-1}$)
S_a	Arithmetical mean height – roughness (μm)
S_{ku}	Kurtosis – roughness (μm)
S_{mp}	Mean distance between peaks – roughness (μm)
S_{pv}	Maximum pit height – roughness (μm)
S_q	Root mean square height – roughness (μm)
S_{sk}	Skewness – roughness (μm)
T	Temperature (°C or K)
x, y	Cartesian positions at the test section plane (m)
z	Vertical position, perpendicular to the test section (m)
$\|\mathbf{g}\|$	Gravitational acceleration magnitude (m s^{-2})

Greek Symbols

β	Static contact angle (°)
ΔT	Superheating degree (K)
δ_1	Slope of curves $\Delta T(P_r)$
δ_2	Slope of curves $\Delta T(CHF)$
ϵ	Uncertainty of the reported magnitude
κ	Thermal conductivity of the test section (W $m^{-1}K^{-1}$)
μ	Dynamic viscosity (Pa s)
∇T	Thermal gradient (K m^{-1})
ν	Kinematic viscosity (m^2s^{-1})
ϕ	Heated surface inclination (°)
ρ	Density (kg m^{-3})
σ	Surface tension (N m^{-1})

Subscripts/Superscripts

CHF	At the critical heat flux point
g	Related to the gas phase
i	Least squares discrete value
κ	Related to thermal conductivity uncertainty
l	Related to the liquid phase
sat	Saturated properties
T	Related to temperature uncertainty
w	At the boiling surface
x	Related to distance uncertainty
$Zuber$	From Zuber's correlation

on the basis of already published works. Note that most publications are concerned with pool boiling enhancement; however, they are not concerned with the texture of the plain surfaces taken as reference. For example, Hu et al. [11] reports plain surfaces with roughness greater than 1 μm, and for some others [12–14] we did not find the roughness of their plain surfaces. It is also interesting to see how some other Refs. Yu et al. [15] reach a roughness of 0.038 μm for a copper test section polished with a 5000 grit emery paper. In addition, Fan et al. [16,17] produced a roughness of 0.019 μm, but did not provide the final polishing grit. Fortunately, Fan et al. [16,17] worked with a test section large enough (circle of 40 mm diameter) to simulate an infinite boiling surface.

The dielectric fluid HFE-7100 is also interesting for its high wettability. Fan et al. [17,18] provided a static contact angle below 12° for copper/HFE-7100 polished (roughness 19 nm) surface. In the same manner, Fariñas Alvariño et al. [10] provided a contact angle for the polished brass surface (roughness 23 nm) of about 5°. Cen et al. [19] also provided a contact angle of 14° for HFE-7100 on copper, and 12.6° was reported by Jiang et al. [20]. A summary of contact angles for different combinations of surfaces/fluids can be found in Mahmoud and Karayiannis [2]. It becomes apparent that fluid HFE-7100 in polished surfaces yields a very small contact angle and, moreover, it becomes null for small roughness values [10]. Therefore, HFE-7100 can be considered a benchmarking fluid with very high wettability. This feature is of utmost importance for numerical scientists interested in comparing their results with experimental evidence [21–24]. Recall that imposing the contact angle on numerical algorithms constitutes a significant source of uncertainty [25].

Conducting pool boiling experiments under different saturation pressures is also necessary to characterize the heat transfer performance of the boiling phenomenon. Yu et al. [15] reported the boiling curves of HFE-7100 on a smooth copper surface under subatmospheric pressures (0–100 kPa). Regrettably, they did not provide the uncertainty of the superheating degree of the boiling surface. Wang et al. [13,26] tested KEY-116 fluid on a copper surface with a roughness of 0.5 μm between 40 and 120 kPa. They provided a wall superheat uncertainty below 8,70% for even more than 50 K. It is interesting to note that experimental uncertainty is of utmost importance to confront experimental results from different laboratories and, mainly, to provide numerical scientists with reliable information to compare with their models.

An additional concern is related to the texture of the boiling surface. Note that previous references were concerned with plain/bare surfaces with different roughness values. However, all of them were polished with emery paper of different grits. Thus, the texture of the polished surface is determined by the polishing direction, and therefore, the boiling surface cannot be considered isotropic. In this regard, laser facilities can produce structured surfaces that might provide useful information on bubble nucleation. Wang and Liang [27] used a nanosecond laser to produce surfaces with micropillars of different sizes and spacing. The working fluid was saturated water at 100 kPa on a 10 × 10 mm copper surface. Ye et al. [28] were concerned with the enhancement of DI water boiling curve on a copper surface. They combined the microstructure produced by the femtosecond laser with a graphene oxide nanocoating obtained from the nanofluid boiling method. Lee et al. [9] studied the enhancement promoted by micro/nano ripple structures produced by a femtosecond laser on a copper boiling surface

Table 1
Summary of some literature works regarding the pool boiling of HFE-7100 fluid.

Work	Operating conditions	Subject
El-Genk [30]	Smooth copper, 85 kPa	Effect of the inclination angle
Misale et al. [31]	Smooth copper, atm. pressure	Effect of inclination angle and gap with inclined narrow spaces
Misale et al. [32]	Smooth copper, atm. pressure	Effect of gap and diameter of unheated surface with narrow spaces
Fariñas Alvariño et al. [10]	Smooth and unstructured rough brass, 25 kPa–200 kPa	Effect of roughness and saturation pressure
Kiyomura et al. [33]	Structured rough copper, 98 kPa	Effect of microfin surfaces
Fan et al. [16]	Smooth copper, 70 kPa–200 kPa	Effect of saturation pressure
dos Santos Filho et al. [34]	Structured rough copper, atm. pressure	Efect of microfins and nanostructures
Fan et al. [18]	Copper and titanium, both structured and smooth, atm. pressure	Effect of titanium dioxide (TiO2) nanotubes
Jiang et al. [20]	Polished and structured rough copper, atm pressure	Effects of microporous coating surfaces
Fan et al. [17]	Polished and unstructured rough copper, 70 kPa–200 kPa	Effect of roughness and saturation pressure
Wu et al. [35]	Structured ITO, atm. pressure	Improvement in the onset of the nucleate boiling whit honeycomb porous plate and heated fine wire
Mlakar et al. [36]	Structured and unstructured rough copper, atm. pressure	Effect of structured and/or unstructured roughness
Yu et al. [15]	Smooth copper, 0.89 kPa–97.1 kPa	Effect of low pressure

with DI water as the working fluid. In the same manner, Lee et al. [9] used a femtosecond laser to produce a set of surfaces that, in some cases, inverted the boiling curve. It is quite interesting how moderated peaks on the surface (about 120 μm) produce a strong enhancement of the CHF.

It is not straightforward to identify the temperature of the boiling surface at the CHF. Fariñas Alvariño et al. [10] showed that, for low pressures and smooth surfaces, some boiling curves attain the CHF after a long excursion of superheating with almost no change in heat flux. The previous statement is also shown by Wang et al. [26] to a lesser extent. However, some experimental setups are not designed to detect this kind of pattern [9,27,29]. Thus, it is widely accepted that CHF is determined prior to the temperature excursion. This research will also demonstrate why this assumption is questionable as a general rule. As previously stated, determining the CHF temperature of the boiling surface is also of utmost importance for both industrial and research purposes.

Table 1 presents a summary of the literature works focused on the HFE-7100 pool boiling study, including the tested operating conditions and the main subjects of the papers. Most references in Table 1 report results at atmospheric pressure, or for a range of pressures so close to it. Only some of them reported results for other pressures than the atmospheric pressure [10,15–17]. Besides, only two of the references in Table 1 provide combined information on the effect of saturation pressure and surface texture. One of these two references is a previous work from the authors [10], which reports the boiling curves for a set of four brass grinded surfaces. The second work [17] studied copper surfaces treated with four different sandpapers, but not with structured surfaces.

Concerning structured and unstructured surfaces, this manuscript provides information for a wider range of saturation pressures than reported in previous references (Table 1), 25 kPa, 50 kPa, 100 kPa and 200 kPa. Note that results at very low subatmospheric pressure, such as 25 kPa, are scarce in the open literature, even more when considering structured surfaces. In addition, the influence of the surface texture at low pressures is almost unexplored. Indeed, none of previous references faces the decreased influence of surface roughness for low pressures. This manuscript shows that this influence is almost negligible for low pressure.

Another contribution of the present work is the analysis of the superheating degree in which the CHF occurs and how the pressure and roughness impacts on it. Despite being already reported in the boiling curves of previous publications, there is no explicit analysis of ΔT_{CHF} *versus* pressure. Meanwhile, this information is presented and discussed in this work.

One should note that the knowledge of how the performance of a boiling surface changes with both pressure and roughness becomes significant for electronic applications (dielectric fluid) intended to keep the electric/electronic devices below a given temperature. If the target temperature is low (e.g. 50 °C), the behavior at low pressures becomes of utmost importance. This temperature is about the CHF of the surface P1200 at 25 kPa. Therefore, applications at low pressures seem to be relevant for engineering purposes, which is covered by the present work.

Through the experimental study of saturated pool boiling of HFE-7100 at four saturation pressures (25, 50, 100, and 200 kPa), our work addresses the impact of reduced pressure (P_r) on pool boiling heat transfer. The impacts of surface roughness are also investigated, considering a polished surface as a reference, three additional surfaces grinded with sandpaper, and two more surfaces with structures created using a laser. The grinded surfaces allow for the analysis of the impact of random structures on pool boiling heat transfer, while the laser structures provide insights about the changes that can be artificially introduced to the pool boiling regime. Our results also provide an illustration of the importance of having a sufficiently large surface of the test section for a correct pool boiling characterization. Here, we report not only the CHF values for each operational condition (pressure-surface), but also the wall superheating at this point with its corresponding uncertainty, which is not quite common in the literature.

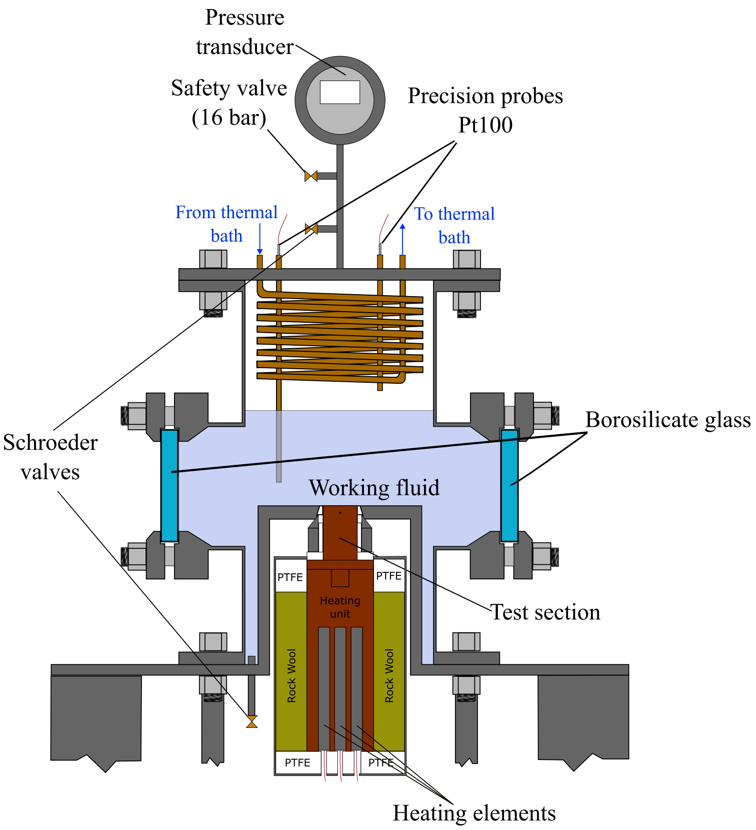

(a)

(b)

Fig. 1. (a) Illustration of the boiler facility used on the experiments. (b) Scheme of the test section with the positions of the thermocouples' holes marked (d_1 and d_2).

Section 2 of this research will report the experimental setup, the boiling vessel, the test section features, and the data processing. Section 2 will also provide the description of the femtosecond laser and its operational features. Section 3 will provide the texture of the boiling surfaces, a critical benchmarking, the yielded boiling curves, and the analysis of the results. A summary of conclusions will be reported in Section 4.

2. Methodology

The boiler description has already been reported by Fariñas Alvariño et al. [10],Martins et al. [25,37]. However, for a better understanding, some features of the experimental facility will be described in this section. A schematic image of the boiler facility is depicted in Fig. 1(a). The boiler is a cylindrical vessel with two circular, opposite windows made of borosilicate glass for the visualization of the test section.

From the top of the chamber, two copper sealed tubes allow the measurement of the gas and liquid phase temperatures using Pt100 precision probes. A JUMO pressure transducer at the top of the chamber measures the pressure inside the boiling vessel. Two Schroeder valves placed at the top and bottom of the boiler serve to fill and drain the working fluid, as well as degassing. Distilled water from a thermal bath passes through a copper serpentine at the upper part of the boiler cylinder to control the internal temperature of the boiler. At the external wall of the boiling vessel, electric flexible heaters are placed to act as an auxiliary heater, helping to achieve the desired operational conditions before starting the experiments. The test section and the two windows are sealed using PTFE gaskets.

The heat unit is composed of a cylindrical copper core with three covered holes, in which three heating elements are placed. The copper core is insulated from the steel cask by two PTFE coverings at the top and bottom, while rock wool is placed between the cylindrical core and the steel cask. The test section is placed at the top of the copper core, with thermal paste between them to ensure a uniform distribution of the heat flux.

An illustration of the test section can be seen in Fig. 1(b), while actual pictures of the used test sections are shown in Fig. 3, machined from a copper rod (Cu-Electrolytic Tough Pitch R300 – Cu> 99.9%). Four holes are drilled from the outside to the center of the cylindrical test section, intended for inserting T-type thermocouples. The consecutive holes were drilled with an angular offset of 90° to avoid heat flux distortion. The boiling surface of any given test section was polished and treated with sand paper to yield the texture shown in Figs. 3 and 4.

Each subsequent surface treatment erodes the test section, reducing the distance from the boiling surface to the first thermocouple. Then, the distance between the first hole and the test section surface is designated as d_1. The other three holes are spaced $d_2 = 5$ mm from each other along the axis of the test section, as one can see in Fig. 1(b). The boiling surface (the upper surface of the test section) is a circle with a diameter of 30 mm for all test sections.

The measured temperatures provide the thermal gradient within the test section, see Appendix A for uncertainty determination. The thermal gradient is defined as the slope of the Least Squares Method (LSM) as:

$$\nabla T_z = \frac{-3T_1 - T_2 + T_3 + 3T_4}{10 d_2}. \tag{1}$$

In the same manner, the temperature of the boiling surface is determined by the offset of the LSM:

$$T_w = -d_1 \nabla T_z + \frac{7T_1 + 4T_2 + T_3 - 2T_4}{10}. \tag{2}$$

This research also focused on the thermal conductivity of the test section. Its value was experimentally yielded and reported in Martins

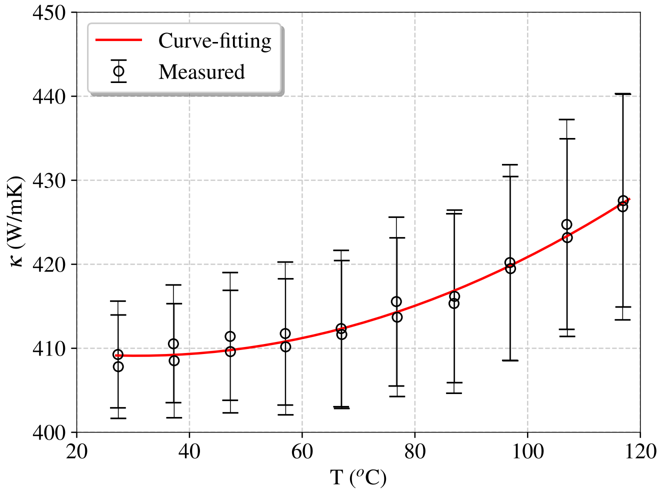

Fig. 2. Thermal conductivity with temperature, considering the copper used to manufacture the test section, and curve fitting used in the acquisition code.

et al. [37], and it is also shown in Fig. 2. The assessment of the corresponding uncertainty is reported in Appendix A.

Again, a least squares procedure yielded the parabolic correlation for the thermal conductivity of the test section, κ, which is also overlaid in Fig. 2. The correlation coefficients were determined according to a parabolic fit,

$$\kappa = a_\kappa T^2 + b_\kappa T + c_\kappa; \tag{3}$$

yielding $a_\kappa = 2.444 \cdot 10^{-3}$, $b_\kappa = -0.150$, and $c_\kappa = 411.410$. Thus, the average temperature of the test section was used to estimate the thermal conductivity for each operating condition. The uncertainty of the copper conductivity was also considered in this experiment through a parabolic fit, as explained in Appendix A.

The conduction Fourier law was subsequently used to determine the heat flux through the boiling surface. The heat flux was determined as:

$$\dot{q}'' = \kappa \nabla T_z. \tag{4}$$

Different surface treatments were applied to each test section shown in Fig. 3. Fig. 3(a) shows the polished test section. The polishing procedure was carried out with a Struers-Labopol facility. The last sandpaper was a silicon carbide P500 foil. Afterwards, the polishing procedure was concluded with a suspension of 1 μm diamond particles. Figs. 3(b), 3(c), and 3(d) illustrate the test sections grinded with emery paper P1200, P220, and P80, respectively. Finally, Figs. 3(e) and 3(f) show the test sections with two different femtosecond laser treatments.

Pictures shown in Fig. 4 were taken with a microscope from the company Dino-Lite with a RK-10-PX mounting device. Fig. 4(a) shows the polished texture, and Figs. 4(b), 4(c), and 4(d) show the grinded finish with P1200, P220, and P80 emery paper, respectively. Fig. 4(e) shows the first laser treatment, which is clearly directional, whereas Fig. 4(f) illustrates the laser treatment intended to be more isotropic. Note that the surface of Fig. 4(f) is far from isotropic; however, it is expected to behave in a different manner than directional textures. Note, as expected, that Figs. 4(b), 4(c), and 4(d) show that the grinding procedure produces textures that are clearly directional, even though the marks from the sandpaper occur in many directions. Besides, Fig. 4(e) shows a strongly directional treatment, which might be considered a benchmark for non-isotropic surfaces. The opposite should be expected from the texture in Fig. 4(f), where the structure of the surface is less dependent on the chosen direction.

It is interesting to stress that the structures shown in Figs. 4(e) and 4(f) have a typical length, about 33 and 40 μm, respectively. Previous works by the same authors provide the size, as well as some other features of single bubbles of HFE-7100. The detachment diameter of a single bubble on a polished copper surface in saturated conditions at 58,3 kPa is about 1500 μm, with a maximum dry diameter of about 1200 μm [37]. In the same manner, the detachment diameter of a single bubble at 195 kPa was about 260 μm, and a maximum dry diameter of about 140 μm [25]. Thus, the typical size of one bubble is one order of magnitude larger than the size of the surface structure. This is, in some ways, a similar feature to those related grinding procedures, but with a more controlled pattern.

The laser used was the Spirit system from Spectra Physics, emitting at a wavelength of 1040 nm and with a pulse width of less than 400 fs. The laser output had a near-Gaussian intensity profile ($M^2 < 1.2$) and a beam diameter of 1.5 mm at the laser head exit. The laser beam has a horizontal polarization (> 100:1). The pulse rate can be adjusted from a single shot up to 1 MHz, with a maximum pulse energy of 40 μJ at 100 kHz. The maximum average output power exceeds 4 W. To scan the laser beam in the X-Y direction, a two-mirror galvanometric scanner (Raylase SuperscanIII-15) was utilized. The beam was focused to a diameter of 30 μm using an F-theta objective lens with a focal length of 160 mm. At the working plane, the beam polarization is parallel to the Y direction. The samples undergo processing in ambient air, and the laboratory's extraction system is utilized to eliminate gases and particles produced during ablation.

The laser was applied to polished surfaces, generating two different structures. For a structure with marked directionality, Structured 1, the laser travels along the surface following parallel lines (along the X axis) at a constant speed. The separation between lines was 30 μm (along the Y axis) and the speed is 30 mm s^{-1}, so that at a frequency of 20 kHz, the overlap along the groove (X axis) is approximately 20 shots. To generate a structure with low directionality, Structured 2, shots were fired at fixed points arranged in a honeycomb pattern. The minimum separation between craters was 80 μm microns, and 40 shots were fired at each one.

Regarding the preparation of the boiler for the experiments, first, a vacuum pump (Telstar model 2F) is used to remove the air inside the boiling chamber. Next, the working fluid (HFE-7100) is suctioned into the boiler up to the required level. Once filled, the test section is heated until the fluid begins to boil. The system is allowed to boil for several minutes to remove any non-condensable gas dissolved in the liquid and to ensure proper degassing inside the vessel.

For operating conditions below atmospheric pressure, the vacuum pump is used to remove gas from the upper part of the boiling chamber. This procedure is gradually repeated until the liquid and gas phases achieve the same temperature, which also matches the expected saturation temperature. This ensures that the working fluid is saturated. For conditions above atmospheric pressure, the vacuum pump is no longer required. The gas is gradually released, taking advantage of the upper Schroeder valve; see Fig. 1(a). Note that, since the boiler vessel is sealed, once degassed there is no need to perform the previous procedure again. Thus, to change the operating conditions (e.g., from high to low pressures), one only needs to heat or cool the boiler system.

As a final remark, the procedure to raise each boiling curves consists of two stages. In a first stage, we drive the boiler close to the CHF. This condition ensures that all cavities on the boiling surface are active. Then, we start to record the experimental data, and progressively reduce the power supply until the natural convection regime is reached. In the second stage, we drive the system again close to the CHF point (the initial condition of the first stage) and then start to collect additional data. Next, the power supply is gradually and carefully increased until the system shifts to film boiling. At this point we switch off the acquisition system and the boiler. The proposed procedure identifies, in a non-questionable manner, the uppermost point of the boiling curve. This maximum was identified as the CHF. This procedure is made in order to confirm the CHF point.

(a) Polished (b) Emery P1200 (c) Emery P220 (d) Emery P80 (e) Laser 1 (f) Laser 2

Fig. 3. Test sections with different boiling surface treatments.

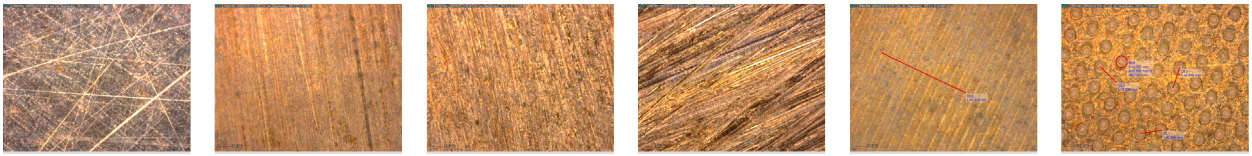

(a) Polished (b) Emery P1200 (c) Emery P220 (d) Emery P80 (e) Laser 1 (f) Laser 2

Fig. 4. Microscopy of the boiling surfaces.

Table 2

Roughness values for all the probes used in the experiments.

Test section	S_a (μm)	S_q (μm)	S_{pv} (μm)	S_{sk} (μm)	S_{ku} (μm)
Polished	0.024 ± 0.005	0.033 ± 0.006	3 ± 1	3 ± 4	300 ± 400
Sandpaper 1200	0.33 ± 0.03	0.44 ± 0.04	7.3 ± 0.9	0.4 ± 0.3	4.9 ± 0.6
Sandpaper 220	0.89 ± 0.08	1.2 ± 0.1	14 ± 3	0.3 ± 0.4	4.6 ± 0.8
Sandpaper 80	1.1 ± 0.10	1.4 ± 0.2	16.7 ± 6.3	-0.1 ± 0.2	3.9 ± 0.4
Structured 1 (grooves)	0.56 ± 0.01	0.65 ± 0.01	6.5 ± 0.9	0.20 ± 0.03	2.04 ± 0.08
Structured 2 (holes)	0.62 ± 0.03	1.01 ± 0.02	9.3 ± 1.0	-2.8 ± 0.1	10.3 ± 0.8

3. Results

3.1. Characterization of the boiling surfaces

The boiling surfaces were also explored with an interferometric microscope Zygo NewView 600 with an objective magnification of 20× (field of view 349 μm × 262 μm, resolution 640 × 480 pixels) and a Z-scan resolution of 0.1 nm. To characterize each boiling surface, five measurements were taken at separate points on the surface, yielding surface roughness parameters according to ISO 25178. The roughness obtained, along with the corresponding uncertainty, is reported in Table 2. The textures of the grinded and laser-treated surfaces can be seen in Fig. 5.

Unlike sanded surfaces, laser-generated structures exhibit high regularity and can be characterized by fitting the topographic results to a simple model. In the case of grooves, the projection on the Y axis is fitted to a series of equal Gaussians separated laterally by a fixed distance. The fit provides the height and width of the Gaussians, as well as the spacing between them, obtaining a depth of 1.74 ± 0.05 μm, a width (4σ) of 26.8 ± 0.5 μm, and a spacing of 33.3 ± 0.2 μm. The second structure, holes, fits a hexagonal distribution of two-dimensional Gaussians, which gives a depth of 4.8 ± 0.3 μm, a diameter (4σ) of 34.1 ± 1.1 μm, and a distance between adjacent craters of 79.6 ± 0.9 μm.

Concerning the wettability of the tested surfaces, previous publications reported a value between 0° and 13° for the static contact angle of the HFE-7100, considering smooth and rough surfaces, both structured and unstructured [10,16–18,20]. In general, the rough surfaces tested by the aforementioned authors presented a lower contact angle than the polished surface. However, all values were considerably low and close to each other. Thus, for the boiling curves presented here, one should keep in mind that the effects of high wettability are present for all the tested surfaces.

3.2. Assessment of the boiling experiments

Two benchmark exercises were developed to compare our results with the experimental evidence reported elsewhere. The red line in Fig. 6(a) shows the boiling curve for the polished test section at 100 kPa. This boiling curve seems to be the proper one to compare with the results of other authors, since it was raised at atmospheric pressure. Fig. 6(a) also shows several correlations: [38–41]. Note that the correlation of Rohsenow [38] almost matches the experimental results reported herein. In addition, Fig. 6(a) shows that the boiling curve of the polished test section is within the range of values defined by other correlations. It is important to note that some correlations used here were developed for tubes instead of plane surfaces. Still, they were considered only for a comparative effect regarding the magnitude order of $\dot{q}''$.

The second benchmark exercise compares the CHF obtained for all operating conditions studied with the polished test section. Fig. 6(b) shows in blue color the CHF for the polished test section under the four saturation pressures studied herein. Note that the correlation of Zuber [1], even though it is not shown in the figure, corresponds to a horizontal line at the level of $\frac{CHF}{CHF_{Zuber}} = 1$. Among several other correlations [42–46], Fig. 6(b) also shows recent data from Yu et al. [15],Fan et al. [17],Jiang et al. [20],El-Genk [30],Misale et al. [32],Mlakar et al. [36]. The correlations used here are described in Appendix B.

Regarding the CHF correlation, one can see that the proposition of Kutateladze [42] gives the closest results in comparison to the current experimental data for a polished surface at 100 kPa. However, this correlation does not capture the CHF - P_r trend found in the experiments, which is better captured by Guan et al. [45] correlation for $P_r \geq 0.0224$ and by Yagov [47] correlations for $P_r \leq 0.0224$. Despite differing more than Kutateladze's correlation, both Guan et al.

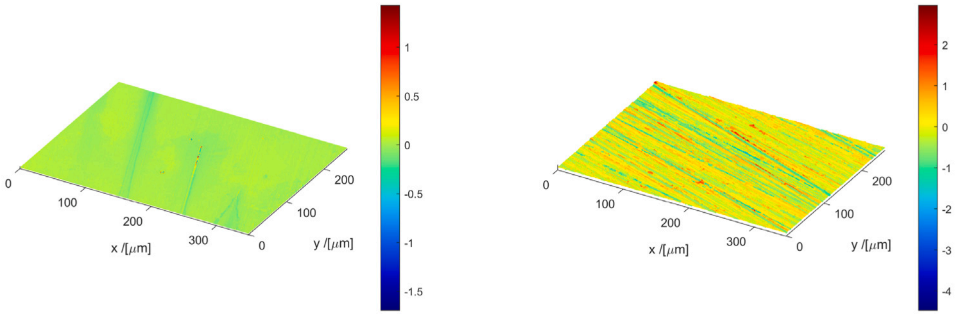

(a) Polished

(b) Emery P1200

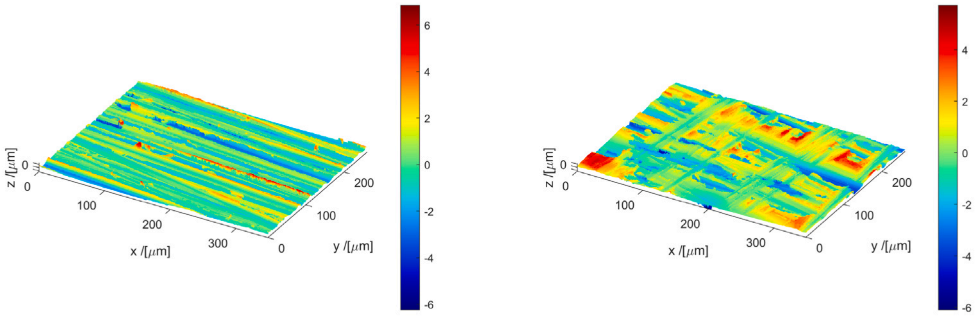

(c) Emery P220

(d) Emery P80

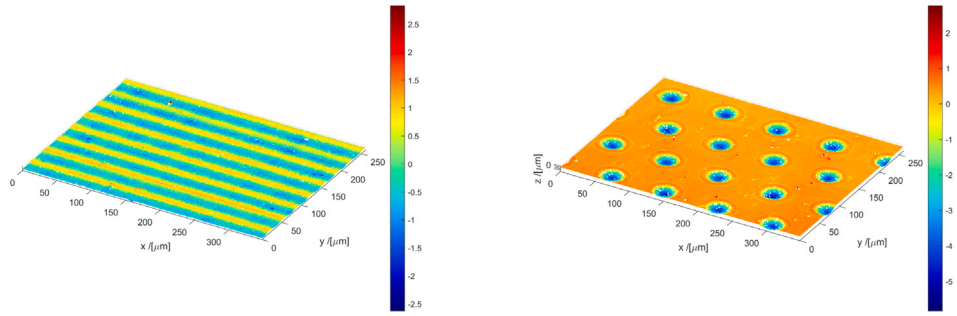

(e) Structured 1 (grooves)

(f) Structured 2 (holes)

Fig. 5. Surface textures colored by height (in μm).

and Yagov correlations are not too far from the current experiments. In general terms, the Kutateladze [42] correlation presented better values in comparison to the experiments, while Guan et al. [45],Yagov [47] correlations presented the better trend of CHF with P_r.

In relation to the experimental results from the literature, the first thing that one can see is that the results of El-Genk [30],Misale et al. [32],Mlakar et al. [36] present higher CHF values than those observed in our experiments. This is because the average roughness of their test section is much higher than the polished surface employed here. While our polished surface achieves $S_a = 0.024$ μm, Misale et al. [32] presented data for $S_a = 0.6$ μm, and Mlakar et al. [36] for $S_a = 0.48$ μm, which are between the average roughness of our test sections treated with P220 and P1200 sandpapers. Also, El-Genk [30] used P1500 sandpaper to polish the copper surface, which should yield a roughness similar to our grinded surface with P1200 sandpaper ($S_a = 0.33$ μm). Thus, when compared to the CHF for our polished surface, 160 ± 9 kW/m^2, their values appear to be much higher, remaining between 222 kW/m^2 and 267 kW/m^2. However, if we compare these values to the CHF for the treated surface with P220 and P1200 sandpapers from our experiments, 256 ± 12 kW/m^2 and 225 ± 10 kW/m^2 respectively, we realize that the values are compatible. If one considers the data uncertainty, they can even be regarded as the same value. The results of Jiang et al. [20] also fit the aforementioned case.

Data from Fan et al. [17] show a similar trend to ours, presenting an increasing CHF value for higher P_r. This trend is also predicted by the correlation of Guan et al. [45]. On the other hand, the data from Yu et al. [15] are above the correlations and experimental evidence from other authors. The heater of Yu et al. [15] was a plate of 20 × 20 mm^2. According to Lienhard and Dhir [8],Lee et al. [9], this enhancement of CHF could be related to the small size of their boiling surface, in case the size of the boiling structures becomes the same order as the heated surface [8,9]. Should this be the case, the CHF increases for a more feasible re-wetting. Besides, data from Yu et al. [15] show a dimensionless increase for very low pressures, which matches the trend reported by our data. Previous comments on the boiling structures can be observed in Figs. 7 and 8.

Regarding the first picture of Fig. 7, with the structures for the polished test section at 100 kPa, we can see that the boiling structures increase in size with increasing heat flux, as expected. The scale of the pictures can be easily estimated since the boiling surface is a circle of

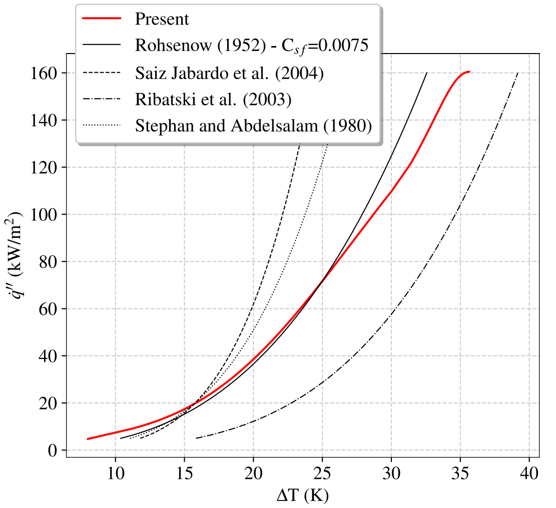

(a) Boiling curve of the polished test section at 100 kPa, and correlations from Rohsenow (1952); Jabardo et al. (2004); Ribatski and Jabardo (2003); Stephan and Abdelsalam (1980).

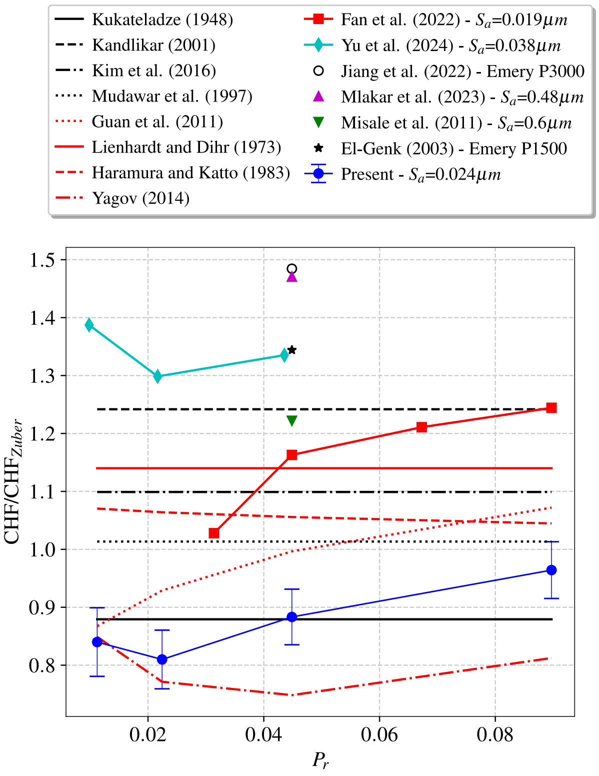

(b) Experimental CHF for polished test section, experimental evidence from other authors El-Genk (2003); Misale et al. (2011); Fan et al. (2022); Jiang et al. (2022); Mlakar et al. (2023); Yu et al. (2024), and correlations on CHF Kutateladze (1948); Mudawar et al. (1997); Kandlikar (2001); Guan et al. (2011); Kim et al. (2016).

Fig. 6. Benchmark exercises.

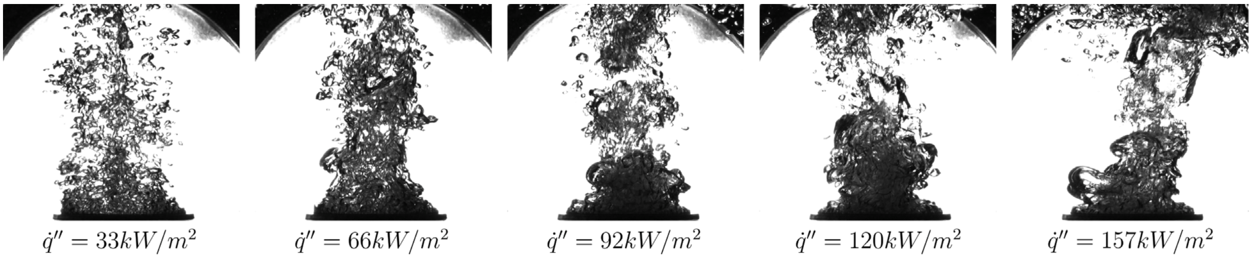

Fig. 7. Multiphase structures for the polished test section at 100 kPa of saturation pressure.

30 mm in diameter. At the beginning of the boiling curve (low heat flux), the nucleate regime is predominant, represented by small bubbles arising from the surface. This regime is identified mostly in the first picture (left) of Fig. 7. As the heat flux increases, larger structures can be progressively visualized. Close to the CHF (the last picture on the right side), the structures seem to be almost the size of the test section. This follows the explanation about the importance of having large enough test sections and the consequences of not having them, as stated by Lienhard and Dhir [8],Lee et al. [9].

Now, regarding Fig. 8, all pictures were taken under CHF for different combinations of saturation pressures and boiling surfaces. It becomes apparent how the boiling structures become larger under low pressures. In addition, it is interesting to observe how, for low pressures (25 kPa) and high heat flux (P80), the size of the boiling structures near the hot surface becomes comparable to the size of the boiling surface. The picture for P80-25 kPa shows three (or even more, given that it is a visual statement) boiling coalesced bubbles very close to the boiling surface. In any case, it can be stated that the size of the boiling structures became the same order as the size of the boiling surface. Under these conditions, it starts to be questionable whether this hot surface is valid for simulating an infinite boiling surface. As stated in the introduction and by Lienhard and Dhir [8].

Previous comparisons show that our data remain within the expected values from the literature references. Thus, further ongoing analysis may be carried out.

3.3. Boiling curves

The boiling curves are reported in Fig. 9. Note that the same axis range was kept for all curves. This feature allows for easy comparison between different curves. Each graphic in Fig. 9 reports the boiling curve for a given surface finish: Fig. 9(a) shows the boiling curves

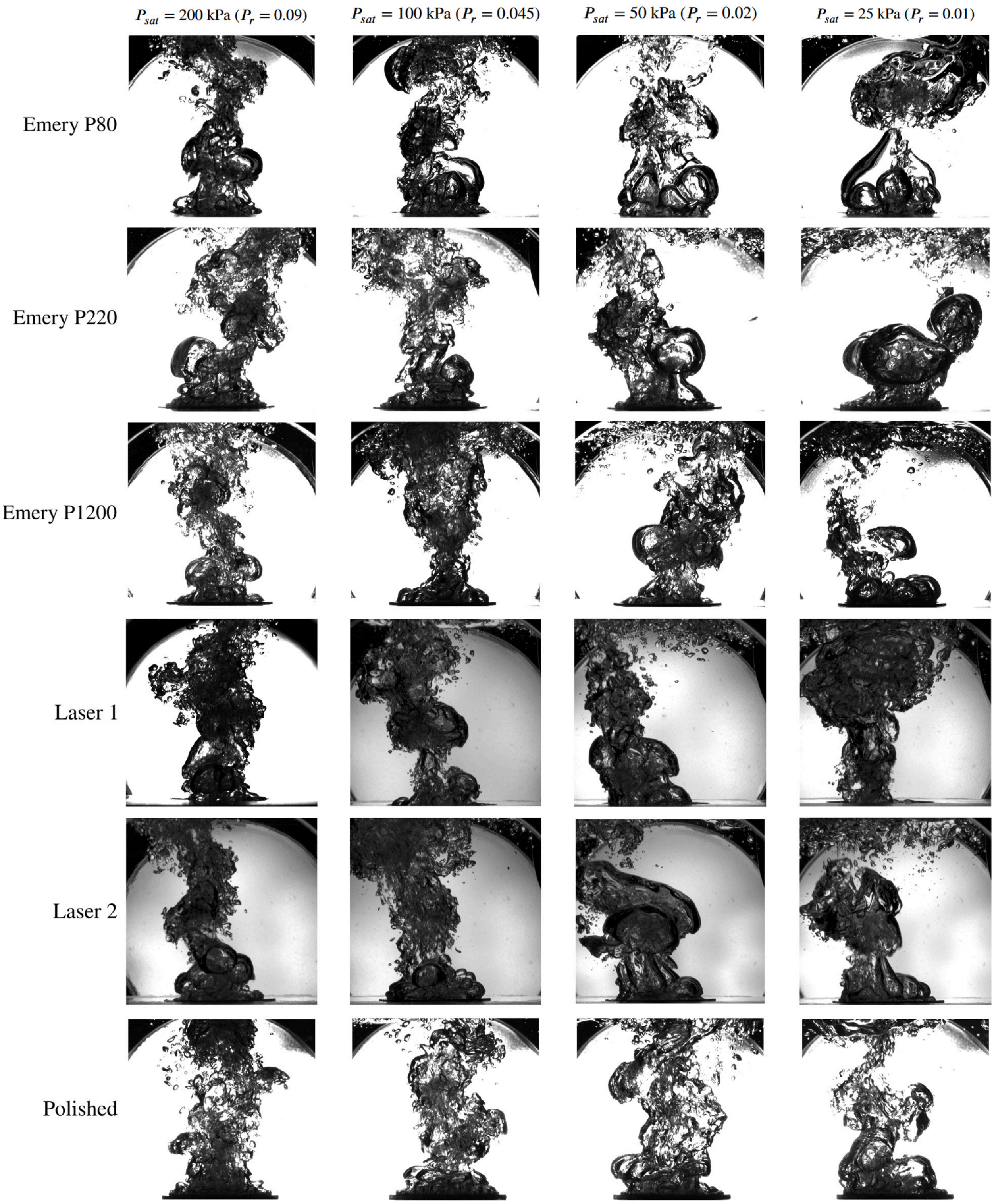

Fig. 8. Pictures of multiphase structures for all surfaces at fluxes near the CHF.

for the polished surface; Figs. 9(b), 9(c), and 9(d) report the boiling curve for the grinded surfaces with P1200, 220 and 80 sandpapers, respectively; finally, Figs. 9(e) and 9(f) provide the boiling curves for the structured surfaces produced by the femtosecond laser.

Several criteria for determining the CHF point can be found in the open literature, ranging from the "burnout point", where the heated filament burns, to the maximum heat flux dissipated by the boiling surface, or a sensitive temperature excursion at the boiling surface. However, our experimental facility allows us to surpass the CHF with the energy supply switched on Fariñas Alvariño et al. [10], and therefore, our facility is not constrained by the temperature excursion of the boiling surface (or the burnout point). Thus, we defined the CHF as the maximum heat flux achieved at the boiling surface without transitioning to the film boiling regime. Fig. 9 plots the boiling curves up to the CHF.

Table 3
Values of CHF with its respective superheating degree for each test section and saturation pressure.

Test section	Saturation pressure (kPa)	CHF (kW/m^2)	ΔT (K)
Polished	25	96 ± 7	41.6 ± 0.3
	50	118 ± 7	39.5 ± 0.3
	100	160 ± 9	35.7 ± 0.4
	200	213 ± 11	29.7 ± 0.4
P1200	25	111 ± 5	29.6 ± 0.2
	50	155 ± 10	26.9 ± 0.4
	100	225 ± 10	30.2 ± 0.4
	200	286 ± 12	29.1 ± 0.4
P220	25	133 ± 7	28.2 ± 0.3
	50	179 ± 9	25.1 ± 0.4
	100	256 ± 12	28.6 ± 0.4
	200	340 ± 16	30.2 ± 0.5
P80	25	153 ± 6	47.6 ± 0.3
	50	184 ± 6	30.2 ± 0.2
	100	257 ± 9	30.4 ± 0.3
	200	319 ± 12	32.7 ± 0.3
Femto structured 1	25	111 ± 7	29.1 ± 0.3
	50	154 ± 8	28.0 ± 0.3
	100	219 ± 7	27.4 + 0.3
	200	285 ± 13	28.1 ± 0.4
Femto structured 2	25	113 ± 7	37.6 ± 0.3
	50	143 ± 9	34.8 ± 0.4
	100	206 ± 14	35.0 ± 0.6
	200	266 ± 18	30.5 ± 0.7

A first observation that comes from the boiling curves is that the presence of roughness, being by grinded surfaces or laser surfaces, increases the ratio $\dot{q}''/\Delta T$. This feature provides higher heat fluxes for lower superheating degrees, suggesting that a textured surface can dissipate more heat for lower ΔT values of the wall. In other words, roughness can enhance heat dissipation during the pool boiling regime.

Second, for reduced pressures well below the critical point, the dimensional CHF increases with pressure, see Table 3. Note, in addition, that Table 3 also identifies the superheating associated with the CHF. As expected, the superheating decreases with pressure, but it is not a general rule. We avoided the uncertainty bars in Fig. 9 for the sake of clarity. A detailed report on uncertainty can be found in Appendix A.

It is also interesting to observe how, as a general rule, low pressures enhance the superheating for the CHF. Note the outstanding increase of superheat shown in Fig. 9(d) (P80) for 25 kPa. This trend seems to show that low pressures allow for a re-wetting of the boiling surface under stronger temperature differences. This feature can also be observed by the pool boiling structures in Fig. 8.

3.4. Analysis of CHF and superheating

The dimensional values of CHF as a function of saturated pressure and roughness are shown in Fig. 10. Note that for low pressure, the CHF for polished, P1200, and both laser treatments becomes closer; see Fig. 10(a). The previous statement was a prior finding of the authors [10] for a different test section material. Thus, with the P_r reduction, the roughness impact reduces, and the CHF values approach each other. As long as the pressure increases, the CHF is enhanced more by the surface texture, since the curves in Fig. 10(a) diverges from each other at high pressures.

However, we can see that up to a certain point, the surface roughness can have an opposite effect, decreasing the CHF as roughness increases. This suggests that the enhancement caused by surface roughness may have some limit, which has already been stated by other authors in the literature [48]. Also, we can identify a coupled effect of pressure and surface roughness. Higher saturation pressure increases the CHF value; however, it also indicates that the limit beyond the roughness begins to act against boiling enhancement.

Thus, previous statements become relevant to identify (i) the roughness limit under which a surface can be considered smooth, and (ii) that the CHF enhancement of a given surface strongly depends on the saturation pressure.

Fig. 10(b) shows the same data presented in Fig. 10(a), but in a more illustrative fashion to observe the effects of both grinding and laser treatments. Note that the dashed lines in Fig. 10(b) indicate the results for both laser treatments. Fig. 10(b) shows that both laser treatments yield essentially the same CHF, as the uncertainty bars are again overlaid.

As a general rule, our results show that laser surfaces yield smaller CHF than those of grinded surfaces with equal roughness value. Hence, it can be concluded that the re-wetting mechanism is more effective for grinded surfaces than for laser treatment. However, the re-wetting mechanism for surfaces treated with emery paper cannot operate under high superheating values.

However, it must be emphasized that neither of the laser textures behaves like the surfaces crafted with emery paper. Fig. 11(a) shows the superheating degree at which the CHF occurs for each tested surface and reduced pressure (P_r). We can see that, excluding the P80 surface at 25 kPa, the grinded surfaces cannot achieve the CHF for higher ΔT values. On the other hand, the structured surface 2 appears to be capable of it, presenting trends that are almost similar in comparison to the polished surface. At the same time, the structured surface 1 showed behavior similar to that of the grinded surfaces. These statements allow us to conclude that there are some surface structures that can maintain the pool boiling regime stable up to higher ΔT values.

Additionally, Fig. 11(b) shows the values of the CHF in relation to the superheating degree in which it occurs. This figure clarifies that most of the CHF occurs at similar values of ΔT, about 30 K. This observation evidences the following fact, previously stated: grinded surfaces cannot retain high heat fluxes for high superheating degrees. For a deeper analysis of Fig. 11 and the boiling features behind it, the following points arise from the data interpretation:

1. The data in Fig. 11(a) of the CHF's superheating values for all tested surfaces and pressures show two different patterns. The slope of the polished and F.Str.2 surfaces is significantly different to that of other surfaces. Indeed, the slope of surfaces P1200, P220, P80, and F.Str.1 is small, thus $\frac{\partial \Delta T}{\partial P_r}|_{S_a} \approx \delta_1$, with the only exception of the single point for the lowest pressure and P80. However, note that this point is non-conventional. Observation of the boiling curve, Fig. 9(d), shows that ΔT for P80 surface at 25 kPa exhibits a huge temperature excursion at almost the CHF, but prior to attain it. We know that this behavior is not the result of any experimental artifact, since it was repeatable and it also took place for different materials of the test section [10]. Besides, Fig. 11(a) shows a different trend for the Polished and F.Str.2 surfaces. A clear slope for both textures is observable, thus $\frac{\partial \Delta T}{\partial P_r}|_{S_a} \gg \delta_1$ for Polished and F.Str.2 textures.
   There is also another unexpected trend in Fig. 11(a); the spreading of the superheating degree in which CHF occurs decreases with pressure. Thus, for low pressures, this superheating is more dependent on the surface texture than for high pressures. Hence, it can be expressed analytically as $\frac{\partial \Delta T}{\partial S_a}|_{low P_r} \ll \frac{\partial \Delta T}{\partial S_a}|_{high P_r}$.
2. Fig. 11(b) shows the same values as Fig. 11(a), but includes the CHF values. Again, two different trends can be devised depending on the texture of the boiling surface. P1200, P220, P80, and F.Str.1 surfaces exhibit a vertical trend, meaning $\frac{\partial \Delta T}{\partial CHF}|_{S_a} \approx \delta_2$. Besides, the Polished and F.Str.2 surfaces show a finite slope in the right region of the figure. Thus, $\frac{\partial \Delta T}{\partial CHF}|_{S_a} \gg \delta_2$.
3. It is well established that the bubble departure size decreases with pressure. See, for example, Du et al. [49].
4. It is also well known that the density of active sites for a given surface is dependent on pressure [50].

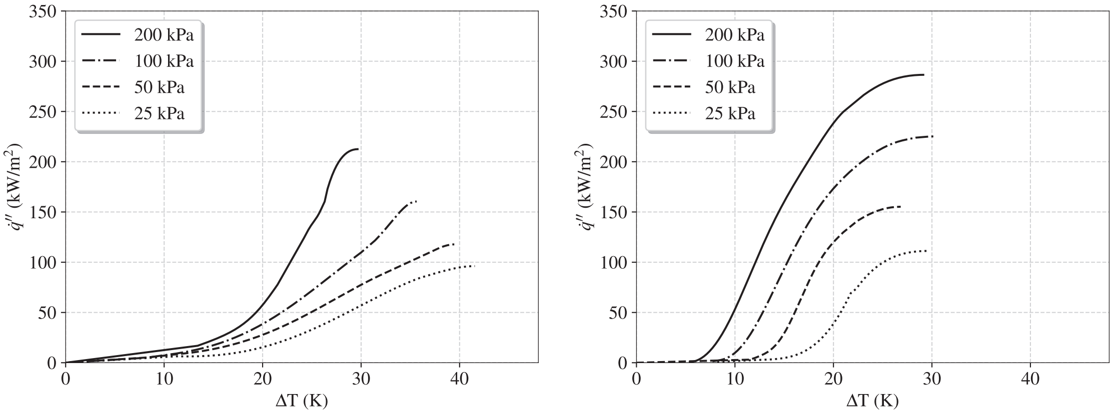

(a) Polished

(b) P1200

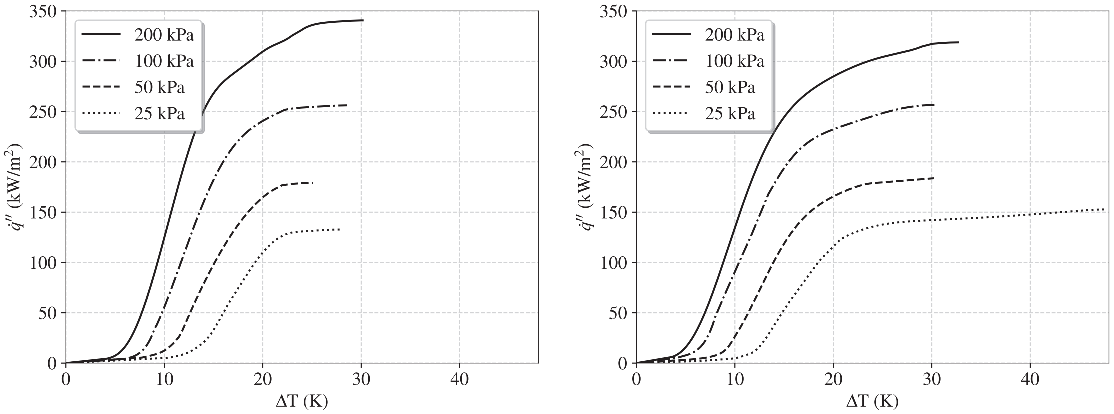

(c) P220

(d) P80

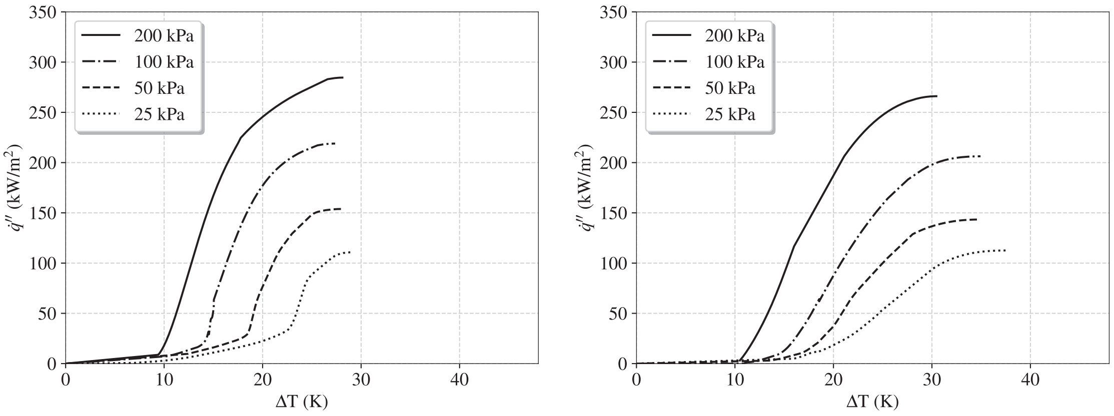

(e) Femto structured 1

(f) Femto structured 2

Fig. 9. Boiling curves for all pressures and surface treatments.

5. An additional relevant parameter is the boiling surface texture. As a general rule, it is also well established that the density of active sites depends on the surface texture. However, two given surface textures that encompasses a wide range and high density of available size of cavities (N_n) might yield a similar density of active sites under equal operating conditions. Thus, for some textures, it is plausible that $\frac{\partial N_n}{\partial S_a}|_{P_r} \approx \epsilon$.
   Note that this expression has the same structure as the final one in point 1. Therefore, it seems that the density of active sites is related to the observed CHF superheating degree.

The overall effect of previous mechanisms is shown in Fig. 8. This array of pictures shows the two-phase boiling structure at CHF for all textures and pressures reported in the paper. It is interesting to note how different is the two-phase boiling structure between the first (P80) and last (Polished) rows. It becomes apparent that the yielded structure is affected by both the surface texture and pressure.

As mentioned before, observation of Fig. 11(a) suggests that Polished and F.Str.2 surfaces behave under the same pattern. Besides, Fig. 11(a) also shows that surfaces P1200, P220, P80, and F.Str.1 collectively behave under a similar trend. Both patterns are also observable

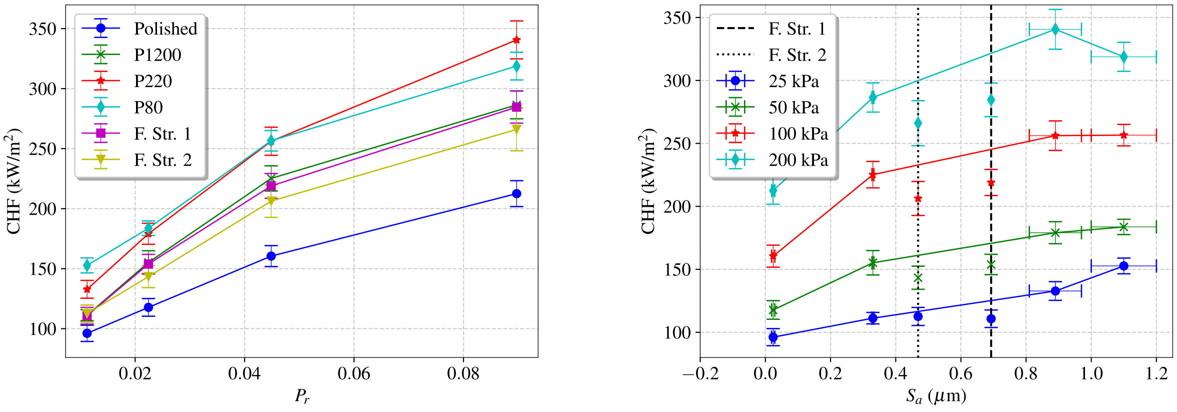

(a) (b)

Fig. 10. CHF as a function of pressure (a) and surface roughness (b).

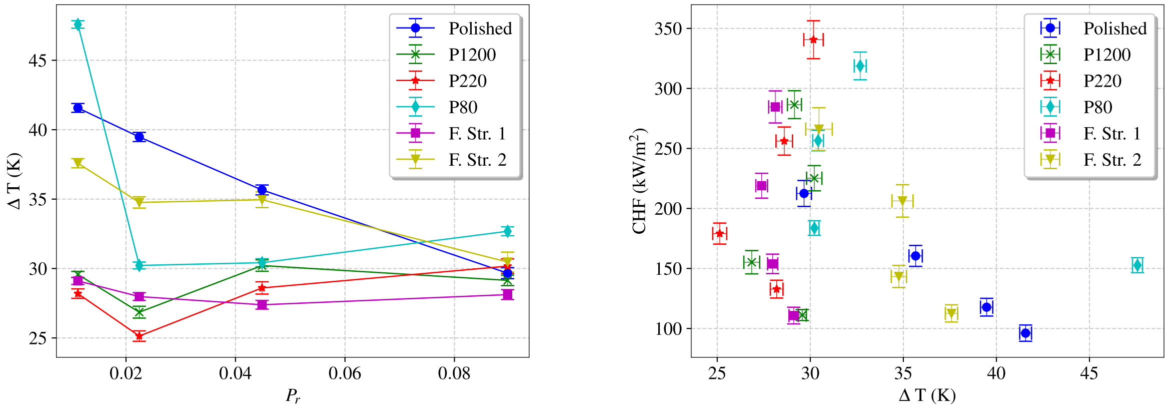

(a) (b)

Fig. 11. Superheating degree where CHF occurs (a) and CHF per superheating degree (b).

in the two-phase boiling structure reported in Fig. 8. In this figure, rows for Polished and F.Str.2 surfaces show a qualitatively similar multiphase structure between each other. Besides, rows for F.Str.1, P1200, P220, and P80 surfaces show also a similar structure with, perhaps, the exception of the lowest pressure. Indeed, the P80 surface at 20 kPa shows a huge structure that, for sure, is related to the non conventional pattern of this point in Figs. 11(a) and 11(b).

The yielded superheating values at CHF are subject to the following underlying boiling mechanisms and features: (i) the size of the bubbles are affected by the saturation pressure (ii) density of active sites are also affected by the surface texture and pressure. However, two given surface textures that encompasses a wide range (and high density) of available size of cavities might yield to a similar density of active sites under equal operating conditions. Thus, for some textures it seems plausible that $\frac{\partial N_n}{\partial S_a}|_{P_r} \approx \epsilon$, where ϵ is a small quantity. See, for example, the results for F.Str.1, P1200, P220, and P80 surfaces in Fig. 8.

In this line of thought, the similarity observed between the polished and the F.Str.2 in Figs. 11(a) and 11(b) suggests that the two surfaces are subjected to mechanisms that drives to similar patterns on density of active sites and bubble coalescence. Recall that Fig. 5 shows that surface F.Str.2 is basically a polished surface with equally distributed holes. The similar behavior of F.Str.2 and polished surfaces may be connected to the fact that a large amount of the surface F.Str.2 surface was kept polished. Thus, similar underlying mechanisms that rule the boiling in the polished test section are expected to operate in F.Str.2 surface.

As an additional remark, we can note that F.Str.2 surface is fully different to that of surface F.Str.1, even though they both yield an almost equal roughness value. Thus, it becomes apparent that roughness value cannot characterize, by its own, the mechanical behavior of a boiling surface.

Recalling the trend shown in Fig. 11(a), where the data is significantly more sparse for low pressure, it can be stated that $\frac{\partial \Delta T}{\partial S_a}|_{low P_r} \ll \frac{\partial \Delta T}{\partial S_a}|_{high P_r}$ for the reported data. Given the similar structure of previous expressions, it seems plausible that the density of active sites in the boiling surface plays an important role on the superheating value at CHF.

4. Conclusions

The present work addresses relevant questions concerning the saturated pool boiling phenomenon on both plane and rough surfaces, considering structured and unstructured features, under both low and high values of reduced pressure. After validating the experimental data by comparing the boiling curve and the CHF values with well-established correlations from the literature, we present the following conclusions.

A somewhat conventional pattern was observed: the increase in the reduced pressure has an enhancing impact on the CHF achieved by the surface. However, the superheating degree at which this point occurs does not present significant changes, since most of the data for CHF remains near $\Delta T = 30$ K.

A nonconventional behavior was found for low pressures concerning the roughness impact: The CHF for different roughnesses became closer, as the results for the polished surface, the grinded surface with P1200 sandpaper, and the two structured surfaces presented almost the same CHF, with a descending trend as P_r decreases. Additionally, our results illustrate that the roughness enhancing effect on the CHF decreases with the pressure reduction. This feature shows that roughness does not affect CHF for low pressures, at least under a certain limit. More research is needed in this regard, since characterization of smooth surfaces is still an open issue for pool boiling under a wide range of pressures.

But for higher pressures, as a general rule, we observed that the surface roughness increases the ratio $\dot{q}''/\Delta T$. Together, the CHF also seems to present an increasing trend with the augmentation of surface roughness. However, for the highest roughness values, the CHF does not increase, even showing a decreasing trend.

Regarding the structured surfaces produced by the femtosecond laser, the data evidenced that, depending on the shape/pattern of the structures, they can affect the boiling phenomena differently, even attaining similar CHF values to conventionally grinded surfaces. One structured surface (number 2, in this work) yielded abnormally high superheating degrees, whereas the other (number 1) presented similar values of ΔT for the CHF as for the grinded surfaces.

Previous observations allow for some assumptions about the wetting and re-wetting phenomena that occur in the pool boiling regime: while a grinded surface usually disturbs the re-wetting phenomena, anticipating the instability of the pool boiling regime and consequently the transition to film boiling, some ordered structures can improve it, retarding the transition to film boiling. The outstanding superheating yielded by the second laser treatment shows the same trend as the polished surface.

A final remark of utmost importance is regarding the confidence and reliability of the experimental results. The yielded results with different textures can be very similar under certain operating conditions. In these cases, the uncertainty value is even more relevant than the value itself. Discerning between different, but similar, results was crucial in this work. Otherwise, it could not be concluded that a smooth surface for pool boiling is not only an issue of the surface; it also depends on the operational conditions. Thus, special care must be taken regarding relevant parameters: test section size, operating conditions, surface texture, and uncertainties.

CRediT authorship contribution statement

Ivan Talão Martins: Writing – review & editing, Writing – original draft, Visualization, Validation, Software, Methodology, Investigation, Formal analysis, Data curation, Conceptualization. **Alberto Ramil Rego:** Writing – review & editing, Writing – original draft, Visualization, Validation, Supervision, Resources, Methodology, Investigation, Funding acquisition, Formal analysis, Data curation, Conceptualization. **Pablo Fariñas Alvariño:** Writing – review & editing, Writing – original draft, Visualization, Validation, Supervision, Resources, Project administration, Methodology, Investigation, Funding acquisition, Formal analysis, Data curation, Conceptualization. **Luben Cabezas-Gómez:** Writing – review & editing, Writing – original draft, Visualization, Validation, Supervision, Resources, Project administration, Methodology, Investigation, Funding acquisition, Formal analysis, Data curation, Conceptualization.

Declaration of competing interest

The authors declare that they have no known competing financial interests or personal relationships that could have appeared to influence the work reported in this paper.

Acknowledgments

This study was financed, in part, by the São Paulo Research Foundation (FAPESP), Brasil. Process Number #2021/14338-0, #2022/15765-1, #2023/02383-6 and #2024/21322-0, and in part by the Coordenação de Aperfeiçoamento de Pessoal de Nível Superior - Brasil (CAPES) - Finance Code 001. The authors also acknowledge the support received from CNPq (National Council for Scientific and Technological Development, process 305771/2023-0), and the funding for open access charge from Universidade da Coruña/CISUG.

Appendix A. Uncertainty determination

The temperature distribution in the test section is supposed to be linear. Thus, the least squares method was used to yield both the slope, a, and the offset, b.

$$a = \frac{n\sum_{i=1}^{n} x_i y_i - \sum_{i=1}^{n} x_i \sum_{i=1}^{n} y_i}{n\sum_{i=1}^{n} (x_i)^2 - \left(\sum_{i=1}^{n} x_i\right)^2} \tag{A.1}$$

$$b = \frac{\sum_{i=1}^{n} y_i - a\sum_{i=1}^{n} x_i}{n} \tag{A.2}$$

with the corresponding uncertainties given by:

$$\epsilon_{a_y}^2 = \sum_{i=1}^{n}\left(\frac{\partial a}{\partial y_i}\right)^2 \epsilon_{y_i}^2 = \frac{n}{n\sum_{i=1}^{n} (x_i)^2 - \left(\sum_{i=1}^{n} x_i\right)^2}\epsilon_y^2; \tag{A.3}$$

$$\epsilon_{b_y}^2 = \sum_{i=1}^{n}\left(\frac{\partial b}{\partial y_i}\right)^2 \epsilon_{y_i}^2 = \frac{\sum_{i=1}^{n} (x_i)^2}{n\sum_{i=1}^{n} (x_i)^2 - \left(\sum_{i=1}^{n} x_i\right)^2}\epsilon_y^2. \tag{A.4}$$

There is, obviously, one source of uncertainty for ϵ_y, which is the uncertainty of temperature inherited from the calibration of thermocouples. However, how good the correlation is constitutes another source for systematic uncertainty. Its characterization can be considered as the root mean square of the residual quantities, thus:

$$\epsilon_y^2 = \frac{\sum_{i=1}^{n}\left[y_i - (ax_i + b)\right]^2}{n-2}; \tag{A.5}$$

where the factor $n-2$ comes from the fact that no errors can be detected from a two-point approach. Eq. (A.5) can be used when data have no available uncertainty and the straight line departs from a perfect correlation. It is a reference to the expected correlation error.

Therefore, in the present investigation, the systematic uncertainty sources arise from: (i) thermocouples measured temperature, (ii) drilled positions and thermocouples location, and (iii) least squares approach accuracy. Even in the absence of temperature and location uncertainties, the temperature points might not attain the same straight line.

Uncertainty propagation from Eqs. (A.1) and (A.2) as a function of the thermocouples location uncertainty, ϵ_x, yields

$$\epsilon_{a_x}^2 = \sum_{i=1}^{n}\left(\frac{\partial a}{\partial x_i}\right)^2 \epsilon_{x_i}^2 = \frac{n\left[n\sum_{i=1}^{n} (y_i)^2 - \left(\sum_{i=1}^{n} y_i\right)^2\right]}{\left[n\sum_{i=1}^{n} (x_i)^2 - \left(\sum_{i=1}^{n} x_i\right)^2\right]^2}\epsilon_x^2; \tag{A.6}$$

$$\epsilon_{b_x}^2 = \sum_{i=1}^{n}\left(\frac{\partial b}{\partial x_i}\right)^2 \epsilon_{x_i}^2 = \left[\frac{a^2}{n} + \frac{\left(\sum_{i=1}^{n} x_i\right)^2}{n}\frac{n\sum_{i=1}^{n} (y_i)^2 - \left(\sum_{i=1}^{n} y_i\right)^2}{\left[n\sum_{i=1}^{n} (x_i)^2 - \left(\sum_{i=1}^{n} x_i\right)^2\right]^2}\right]\epsilon_x^2. \tag{A.7}$$

The systematic uncertainties are calculated according to the classical propagation procedure from Eqs. (1) and (2), Moffat [51], and can be expressed as:

$$\epsilon_{\nabla T_z}^2 = \frac{\left[4\sum_{i=1}^{4} (T_i)^2 - \left(\sum_{i=1}^{4} T_i\right)^2\right]\epsilon_x^2 + 20d_2^2\epsilon_T^2}{100d_2^4}; \tag{A.8}$$

$$\epsilon_{T_w}^2 = \frac{\nabla T_z^2 + \left[4\sum_{i=1}^{4}\left(T_i\right)^2 - \left(\sum_{i=1}^{4} T_i\right)^2\right]\left(\frac{2d_1+3d_2}{10d_2^2}\right)^2}{4}\epsilon_x^2 + \frac{2d_1^2+7d_2^2+6d_1d_2}{10d_2^2}\epsilon_T^2. \tag{A.9}$$

Now, the temperature systematic uncertainty, ϵ_T, must be addressed. One precision (1/10 DIN) Pt100 has been checked and calibrated at ETSII-UPM, see acknowledgements, and compared with a reference probe through immersion in a stabilized thermal bath. Such a comparison was made at −25, 0, 20, 40, 60, and 80 °C observing differences below 0.03 °C for all reported temperatures. Therefore, this precision (1/10 DIN) Pt100 has been adopted as the reference one in the laboratory for this investigation. This reference Pt100 served to calibrate all temperature transducers in the present work. Under these conditions, the chosen systematic uncertainty for the thermocouples/Pt100 probes was $\epsilon_T = 0.1^{\circ}C$.

As previously stated, the drilling hole position to insert the thermocouples was marked through a CNC machining apparatus. As a result, the drilled holes' head location uncertainty is $\approx \pm 1.0exp(-05)m$, which is almost negligible. However, the drilled thermocouple holes were of 1.0 mm diameter, whereas each thermocouple wire is of 0.3 mm. Considering the plastic wire protection, the thermocouples did enter the holes with no slack.

Since the hole diameter is 1.0 mm and the thermocouple wires are both 0.3 mm, it will be assumed an uncertainty in the thermocouple location of $\epsilon_x = \pm 2.0exp(-04)m$.

The last systematic uncertainty source is related to the LSM quality. It is necessary to decide the terms of the maximum allowable deviation concerning LSM to admit the experimental data or, alternatively, how much the uncertainty needs to be increased for a non-perfect correlation.

This research adopted a conservative decision. A test section yielding a low-quality correlation must be discarded, according to the following criteria: (i) In case all four thermocouples match the LS correlation within their position/temperature uncertainty, the experiments were carried out in the regular manner. (ii) In case one of the thermocouples falls out of the correlation to a greater extent than the uncertainty, the probe is discarded, and the experiment goes on with only three reliable thermocouples. In this case, all previous equations are adapted to operate with three thermocouples. And finally, (iii) in case two thermocouples fall out of the correlation, the test section is discarded.

The test section was machined from an electrolytic copper rod. Its thermal conductivity was experimentally measured and compared to the standard one. One piece of material from the rod was utilized to measure its thermal conductivity, and the task was developed at Zaragoza University SAI. The measurements were performed using the TTO option of a commercial PPMS. The TTO system provides the thermal conductivity by measuring the temperature drop along the sample.

As mentioned before, both the thermal conductivity, κ, and its uncertainty, ϵ_κ, can be correlated through a least squares standard procedure to a parabolic equation. For the uncertainty as a function of the temperature in ^{o}C, we have:

$$\epsilon_\kappa = a_{\epsilon_\kappa} T^2 + b_{\epsilon_\kappa} T + c_{\epsilon_\kappa}; \tag{A.10}$$

The adopted coefficients for the κ fitting were already mentioned in Section 2. For the thermal conductivity uncertainty, they were: $a_{\epsilon_\kappa} = 0.00013$, $b_{\epsilon_\kappa} = 0.057$, and $c_{\epsilon_\kappa} = 4.59$. In Fig. A.1, we have the experimental uncertainty measured for copper thermal conductivity and the polynomial fit adopted in this study.

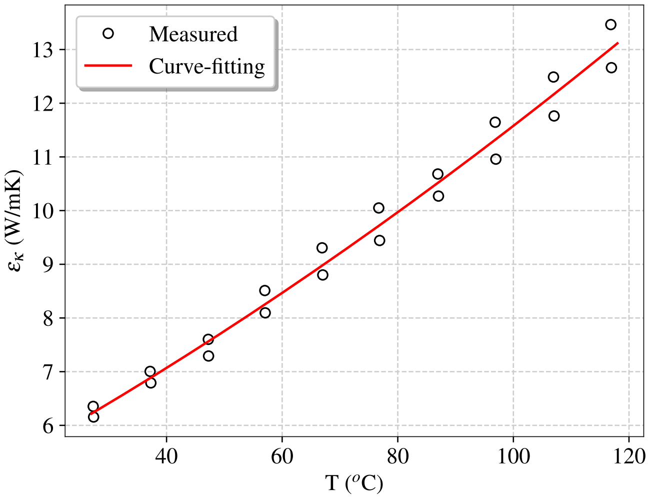

Fig. A.1. Experimental uncertainty of copper thermal conductivity and the polynomial fit adopted in this study.

The only remaining issue is to determine the random uncertainty. In any experimental setup, the random uncertainty is related to the experimental facility and operational methodology. The proposed methodology yielded a negligible random uncertainty, since consecutive experiments provide boiling curves that almost match each other. In any case, random uncertainty is not comparable to the systematic one.

The uncertainty for each measured point of all boiling curves is reported in Figs. A.2 and A.3.

Appendix B. Critical heat flux correlations

In this section, we present the CHF correlations used as a reference for this work. Starting by the correlation proposed by Kutateladze [42], which relates the CHF with gravitational acceleration ($|\mathbf{g}|$), surface tension (σ), latent heat of vaporization (h_{lg}) and liquid/gas densities (ρ_g, ρ_l), as stated by Eq. (B.1).

$$\dot{q}''_{CHF} = 0.1310\rho_g^{0.5} h_{lg}\left[|\mathbf{g}|\sigma(\rho_l - \rho_g)\right]^{0.25} \tag{B.1}$$

The next is the Zuber [1] correlation, which is very similar to Kutateladze [42] correlation, changing only the constant, as given by Eq. (B.2).

$$\dot{q}''_{CHF} = 0.149\rho_g^{0.5} h_{lg}\left[|\mathbf{g}|\sigma(\rho_l - \rho_g)\right]^{0.25} \tag{B.2}$$

Lienhard and Dhir [8] achieved an similar expression for the CHF, but they investigated the effects of the surface extension on the CHF. Giving in terms of Zuber's correlation for the CHF, they find that for an infinite surface the critical heat flux can be given by $\dot{q}''_{CHF} = 1.14\dot{q}''_{CHF,Zuber}$.

Haramura and Katto [52] proposed a set of CHF predictive correlations considering several boiling surfaces and orientations. For an upward-facing horizontal disk, their correlation is given by Eq. (B.3).

$$\dot{q}''_{CHF} = 1.83^{5/16}\left\{\left[2\pi\left(\frac{3\sigma}{g\left(\rho_l - \rho_g\right)}\right)^{1/2}\right]^2 / \left(\frac{\pi}{4}d^2\right)\right\}^{1/16} \tag{B.3}$$

Mudawar et al. [43] also proposed a similar correlation, again changing the constant that multiplies the relation between the parameters, Eq. (B.4).

$$\dot{q}''_{CHF} = 0.151\rho_g^{0.5} h_{lg}\left[|\mathbf{g}|\sigma(\rho_l - \rho_g)\right]^{0.25} \tag{B.4}$$

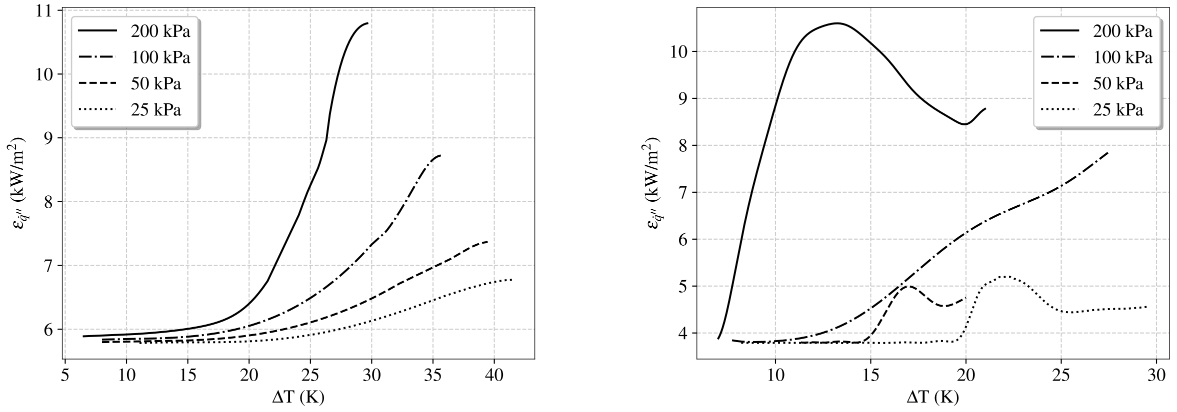

(a) Polished

(b) P1200

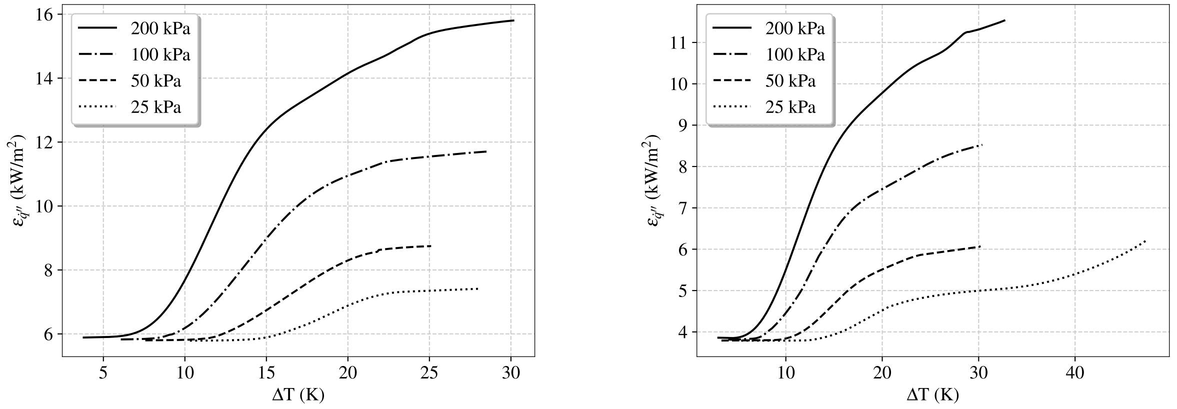

(c) P220

(d) P80

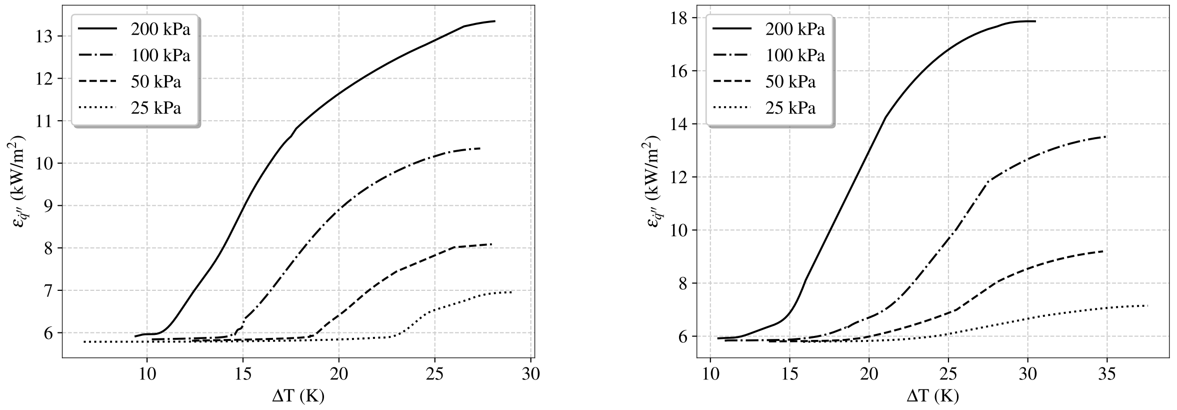

(e) Hydrophobic surface

(f) Hydrophilic surface

Fig. A.2. Heat flux uncertainty for all reported boiling curves as a function of the superheating on the boiling surface.

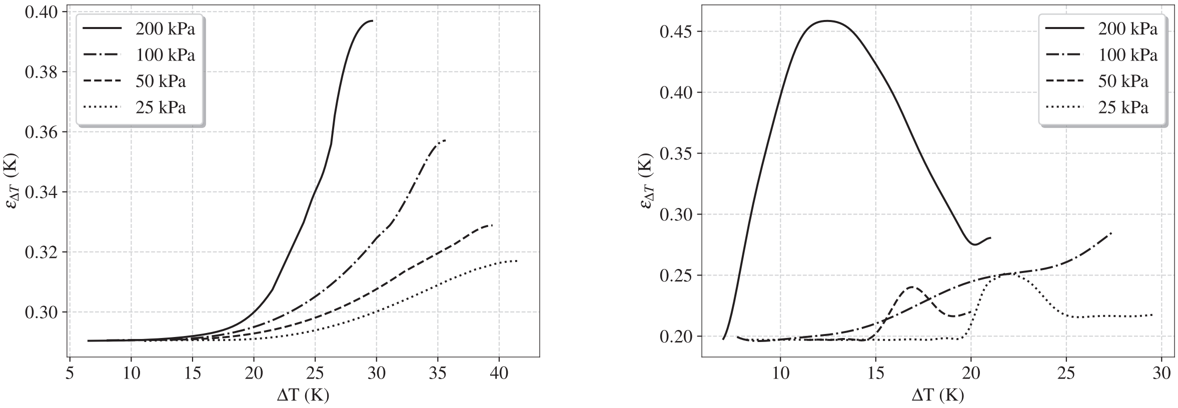

(a) Polished (b) P1200

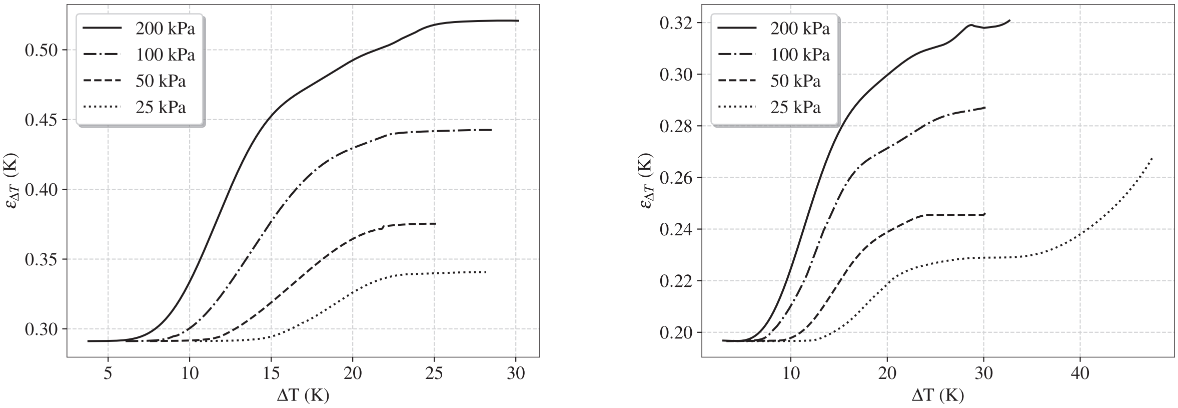

(c) P220 (d) P80

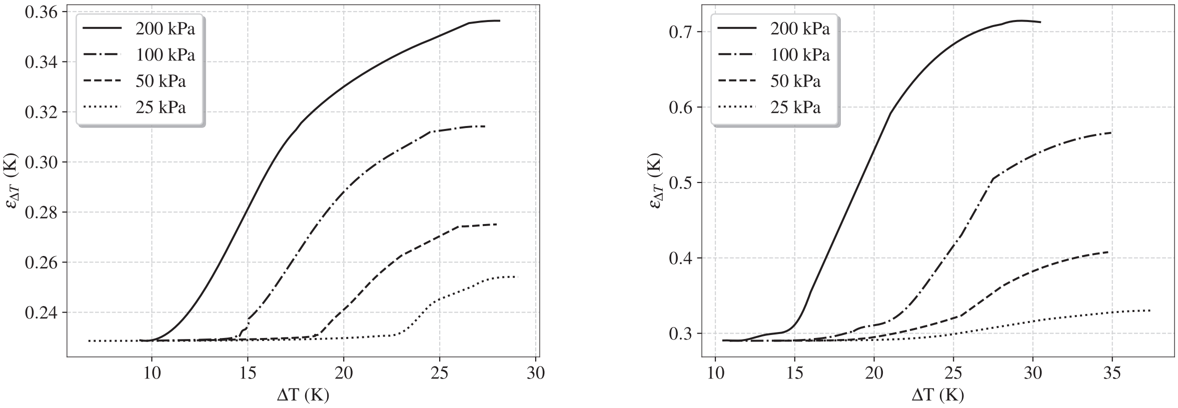

(e) Hydrophobic surface (f) Hydrophilic surface

Fig. A.3. Superheating uncertainty for all reported boiling curves. The uncertainties are reported as a function of the superheating value.

Kandlikar [44]inserts additional effects on the CHF correlation, considering the wettability of the surface through the static contact angle, β, as well as the surface inclination, ϕ, as in Eq. (B.5).

$$\dot{q}''_{CHF} = \left\{ \left(\frac{1+\cos\beta}{16} \right) \left[\frac{2}{\pi} + \frac{\pi}{4}\left(1+\cos\beta\right)\cos\phi \right]^{0.5} \right\} \rho_g^{0.5} h_{lg} \left[|\mathbf{g}|\sigma(\rho_l - \rho_g) \right]^{0.25} \tag{B.5}$$

On the other hand, Yagov [47] added the effects of reduced pressure in a different way, separating two expressions for two distinct regions of P_r. For $P_r > 0.03$, the expression given by Eq. (B.6) is proposed, while Eq. (B.7) should be used for $P_r < 0.001$. In these expressions, Pr is the Prandtl number, while R_i is the gas constant for the working fluid, ν and μ_l are the liquid kinematic and dynamic viscosities, respectively, and Cp_l is the specific heat at constant pressure of the liquid. For the intermediary region, the authors proposed a general expression as

$$\dot{q}''_{CHF,h} = \left[\left(\dot{q}''_{CHF}\right)^3 + \left(\dot{q}''_{CHF,l}\right)^3 \right]^{1/3}.$$

$$\dot{q}''_{CHF,h} = 0.06 h_{lg} \rho_g^{0.6} \sigma^{0.4} \left[\frac{g\left(\rho_l - \rho_g\right)}{\mu_l} \right]^{0.2} \tag{B.6}$$

$$\dot{q}''_{CHF,l} = 0.5 \frac{h_{lg}^{81/55} \rho_g^{13/110} \sigma^{9/11} \kappa_l^{7/110} g^{21/55}}{\nu_l^{1/2} Cp_l^{3/10} R_i^{79/110} T_{sat}^{21/22}} \left(\frac{Pr^{9/8}}{1 + 2Pr^{1/4} + 0.6Pr^{19/24}} \right)^{4/11} \tag{B.7}$$

Kim et al. [46] in their correlation also considered effects of surface roughness, but in this case, they also used the mean distance between peaks, S_{mp}, and the average roughness of the surface, S_a, both in μm, given by Eq. (B.8).

$$\dot{q}''_{CHF} = \left\{ 0.811 \left(\frac{1+\cos\beta}{16} \right) \left[\frac{2}{\pi} + \frac{\pi}{4}\left(1+\cos\beta\right) + 351.2 \frac{\cos\beta}{(1+\cos\beta)} \frac{S_a}{S_{mp}} \right]^{0.5} \right\} \times \rho_g^{0.5} h_{lg} \left[|\mathbf{g}|\sigma(\rho_l - \rho_g) \right]^{0.25} \tag{B.8}$$

At last, Guan et al. [45] correlation was also used, which provides major sensitivity to the reduced pressure due to the density ratio between liquid and gas phases, as already observed before in Fig. 6(b). The correlation is given by Eq. (B.9).

$$\dot{q}''_{CHF} = \left[0.2445 \left(1 + \frac{\rho_g}{\rho_l} \right)^{0.25} \left(\frac{\rho_g}{\rho_l} \right)^{1/10} \right] \rho_g^{0.5} h_{lg} \left[|\mathbf{g}|\sigma(\rho_l - \rho_g) \right]^{0.25} \tag{B.9}$$

Data availability

Data will be made available on request.

References

[1] N. Zuber, Hydrodynamic Aspect of Boiling Heat Transfer (Ph.D. thesis), University of California, Los Ángeles, California, 1959.

[2] M. Mahmoud, T. Karayiannis, Pool boiling review: Part II – heat transfer enhancement, Therm. Sci. Eng. Prog. 25 (2021) 101023, http://dx.doi.org/10.1016/j.tsep.2021.101023, URL: https://www.sciencedirect.com/science/article/pii/S2451904921001840.

[3] M. Mahmoud, T. Karayiannis, Pool boiling review: Part I – fundamentals of boiling and relation to surface design, Therm. Sci. Eng. Prog. 25 (2021) 101024, http://dx.doi.org/10.1016/j.tsep.2021.101024, URL: https://www.sciencedirect.com/science/article/pii/S2451904921001852.

[4] J. Li, Y. Huang, Y. Qiu, S. Wang, Q. Yang, K. Wang, Y. Zhu, Prediction of critical heat flux using different methods: A review from empirical correlations to the cutting-edge machine learning, Int. Commun. Heat Mass Transfer 160 (2025) 108362, http://dx.doi.org/10.1016/j.icheatmasstransfer.2024.108362, URL: https://www.sciencedirect.com/science/article/pii/S0735193324011242.

[5] M.Z. Ullah, Y. Ma, A.A. Ahmad, M. Liu, Pool boiling enhancement on micro- and nano-structured surfaces and fouling mitigating strategies - A review, Int. J. Heat Mass Transfer 238 (2025) 126458, http://dx.doi.org/10.1016/j.ijheatmasstransfer.2024.126458, URL: https://www.sciencedirect.com/science/article/pii/S0017931024012869.

[6] H. Chu, X. Yu, H. Jiang, D. Wang, N. Xu, Progress in enhanced pool boiling heat transfer on macro- and micro-structured surfaces, Int. J. Heat Mass Transfer 200 (2023) 123530, http://dx.doi.org/10.1016/j.ijheatmasstransfer.2022.123530, URL: https://www.sciencedirect.com/science/article/pii/S0017931022009991.

[7] F. Ahmad, M. Meyer, J. Hartwig, I. Mudawar, Saturated pool film boiling of cryogenic fluids: Review of databases, assessment of existing models and correlations, and development of new universal correlation, Int. J. Heat Mass Transfer 235 (2024) 126190, http://dx.doi.org/10.1016/j.ijheatmasstransfer.2024.126190, URL: https://www.sciencedirect.com/science/article/pii/S0017931024010202.

[8] J.H. Lienhard, V.K. Dhir, Hydrodynamic prediction of peak pool-boiling heat fluxes from finite bodies, J. Heat Transf. 95 (2) (1973) 152–158, http://dx.doi.org/10.1115/1.3450013.

[9] S. Lee, Y. Kim, H. Ki, J. Lee, Pool-boiling enhancement on periodic micro/nano ripple-structured surfaces fabricated by femtosecond laser, Int. Commun. Heat Mass Transfer 148 (2023) 107072, http://dx.doi.org/10.1016/j.icheatmasstransfer.2023.107072, URL: https://www.sciencedirect.com/science/article/pii/S073519332300461X.

[10] P. Fariñas Alvariño, M.L. Sánchez Simón, M. dos Santos Guzella, J.M. Amado Paz, J.M. Sáiz Jabardo, L. Cabezas Gómez, Experimental investigation of the CHF of HFE-7100 under pool boiling conditions on differently roughened surfaces, Int. J. Heat Mass Transfer 139 (2019) 269–279, http://dx.doi.org/10.1016/j.ijheatmasstransfer.2019.04.142, URL: https://www.sciencedirect.com/science/article/pii/S0017931018346714.

[11] Y. Hu, D. Fu, S. Hong, Z. Gao, C. Dang, S. Wang, Experimental investigation on pool boiling performance of expanding-microchanneled surface at sub-atmospheric pressure environment, Int. Commun. Heat Mass Transfer 161 (2025) 108408, http://dx.doi.org/10.1016/j.icheatmasstransfer.2024.108408, URL: https://www.sciencedirect.com/science/article/pii/S0735193324011709.

[12] M. Kamali, H. Shakeri, H. Saffari, The effect of hydrophobic teflon pillars with various diameters and spacings on enhanced pool boiling performance: Experiments and empirical correlation, Int. Commun. Heat Mass Transfer 161 (2025) 108491, http://dx.doi.org/10.1016/j.icheatmasstransfer.2024.108491, URL: https://www.sciencedirect.com/science/article/pii/S0735193324012533.

[13] X. Wang, K. Liang, J. Xu, J. Wang, X. Chen, Experimental study on bubble dynamics and heat transfer of pool boiling at sub-atmospheric pressures, Int. Commun. Heat Mass Transfer 148 (2023) 107065, http://dx.doi.org/10.1016/j.icheatmasstransfer.2023.107065, URL: https://www.sciencedirect.com/science/article/pii/S0735193323004542.

[14] K. Yuki, K. Yuki, T. Ogushi, M. Murakami, T. Numata, T. Ide, Key factors affecting the boiling heat transfer coefficient of FC-72 in saturated pool boiling using lotus-type porous copper, Int. J. Heat Mass Transfer 238 (2025) 126477, http://dx.doi.org/10.1016/j.ijheatmasstransfer.2024.126477, URL: https://www.sciencedirect.com/science/article/pii/S001793102401305X.

[15] J. Yu, Z. Chen, Y. Utaka, Critical heat flux characteristics in pool boiling at low pressure for dielectric fluid Novec 7100, Int. J. Heat Mass Transfer 232 (2024) 125959, http://dx.doi.org/10.1016/j.ijheatmasstransfer.2024.125959, URL: https://www.sciencedirect.com/science/article/pii/S0017931024007890.

[16] X. Fan, M.M. Mahmoud, A. Ivanov, T.G. Karayiannis, Saturated nucleate boiling with HFE-7100 on a plain smooth copper surface, in: In Proc. 5th World Congress on Momentum, Heat and Mass Transfer (MHMT'20). Paper No. ICMFHT 123, 2020, pp. 1–9, http://dx.doi.org/10.11159/icmfht20.123.

[17] X. Fan, S. Gu, J. Lei, G. Luo, F. Meng, L. Wu, S. Gu, Experimental and analytical study on the influence of saturation pressure and surface roughness on pool boiling CHF of HFE-7100, Int. J. Chem. Eng. 2022 (1) (2022) 4875208, http://dx.doi.org/10.1155/2022/4875208, URL: https://onlinelibrary.wiley.com/doi/abs/10.1155/2022/4875208.

[18] S. Fan, W. Tong, F. Duan, Nucleate pool boiling heat transfer enhancement in saturated Novec 7100 using titanium dioxide nanotube arrays, Int. Commun. Heat Mass Transfer 122 (2021) 105166, http://dx.doi.org/10.1016/j.icheatmasstransfer.2021.105166, URL: https://www.sciencedirect.com/science/article/pii/S0735193321000609.

[19] M. Cen, S. Deng, C. Hu, J. Luo, S. Tan, C. Wang, Y. Wu, Enhanced boiling heat transfer of HFE-7100 on copper foams under overflow conditions, Appl. Therm. Eng. 224 (2023) 120083, http://dx.doi.org/10.1016/j.applthermaleng.2023.120083, URL: https://www.sciencedirect.com/science/article/pii/S1359431123001126.

[20] Y. Jiang, G. Zhou, J. Zhou, F. Zhou, X. Huai, Saturated pool boiling heat transfer of HFE-7100 on sintered copper powder and wire mesh microporous surfaces: A comparison study, Appl. Therm. Eng. 216 (2022) 119067, http://dx.doi.org/10.1016/j.applthermaleng.2022.119067, URL: https://www.sciencedirect.com/science/article/pii/S1359431122009991.

[21] J. Wang, M. Diao, X. Liu, Numerical simulation of pool boiling with special heated surfaces, Int. J. Heat Mass Transfer 130 (2019) 460–468, http://dx.doi.org/10.1016/j.ijheatmasstransfer.2018.10.120, URL: https://www.sciencedirect.com/science/article/pii/S0017931018324426.

[22] J. Bi, D.M. Christopher, D. Zhao, J. Xu, Y. Huang, Numerical study of bubble growth and merger characteristics during nucleate boiling, Prog. Nucl. Energy 112 (2019) 7–19, http://dx.doi.org/10.1016/j.pnucene.2018.12.001, URL: https://www.sciencedirect.com/science/article/pii/S0149197018302968.

[23] L. Bures, M. Bucci, Y. Sato, M. Bucci, A coarse grid approach for single bubble boiling simulations with the volume of fluid method, Comput. & Fluids 271 (2024) 106182.

[24] F. Ejaz, B. Kwon, Two-phase active immersion cooling for vertically mounted electronics with interchip component-assisted bubble departure, Int. Commun. Heat Mass Transfer 159 (2024) 107981, http://dx.doi.org/10.1016/j.icheatmasstransfer.2024.107981, URL: https://www.sciencedirect.com/science/article/pii/S0735193324007437.

[25] I.T. Martins, L.C. Gómez, P.F. Alvariño, Design and validation of a lattice Boltzmann method with real properties for single-bubble boiling simulation, Int. Commun. Heat Mass Transfer 167 (2025) 109207, http://dx.doi.org/10.1016/j.icheatmasstransfer.2025.109207, URL: https://www.sciencedirect.com/science/article/pii/S0735193325006335.

[26] X. Wang, C. Yang, C. Xu, H. Zhu, X. Chen, K. Liang, J. Xu, Correlation of pool boiling heat transfer and enhancement by microstructure surfaces at sub-atmospheric pressures, Int. J. Heat Mass Transfer 226 (2024) 125465, http://dx.doi.org/10.1016/j.ijheatmasstransfer.2024.125465, URL: https://www.sciencedirect.com/science/article/pii/S0017931024002965.

[27] J. Wang, G. Liang, Experimental investigation of pool boiling performance and bubble behavior on square micro-pillar structured surfaces, Int. J. Heat Mass Transfer 239 (2025) 126556, http://dx.doi.org/10.1016/j.ijheatmasstransfer.2024.126556, URL: https://www.sciencedirect.com/science/article/pii/S001793102401384X.

[28] F. Ye, L. Song, Y. Wang, Y. Yang, R. Jin, J. Jiang, H. Tao, J. Lin, Femtosecond laser-based construction of 3D spatially distributed graphene oxide surface for enhancing boiling heat transfer, Int. J. Heat Mass Transfer 237 (2025) 126405, http://dx.doi.org/10.1016/j.ijheatmasstransfer.2024.126405, URL: https://www.sciencedirect.com/science/article/pii/S0017931024012341.

[29] P. Sen, S. Kalita, D. Sen, A.K. Das, B.B. Saha, Pool boiling heat transfer and bubble dynamics of modified copper micro-structured surfaces, Int. Commun. Heat Mass Transfer 134 (2022) 106039, http://dx.doi.org/10.1016/j.icheatmasstransfer.2022.106039, URL: https://www.sciencedirect.com/science/article/pii/S0735193322001610.

[30] M. El-Genk, Combined effects of subcooling and surface orientation on pool boiling of hfe-7100 from a simulated electronic chip, Exp. Heat Transfer 16 (4) (2003) 281–301, http://dx.doi.org/10.1080/08916150390242244, URL: https://www.tandfonline.com/doi/abs/10.1080/08916150390242244.

[31] M. Misale, G. Guglielmini, A. Priarone, HFE-7100 pool boiling heat transfer and critical heat flux in inclined narrow spaces, Int. J. Refrig. 32 (2) (2009) 235–245, http://dx.doi.org/10.1016/j.ijrefrig.2008.06.003, URL: https://www.sciencedirect.com/science/article/pii/S0140700708001205.

[32] M. Misale, G. Guglielmini, A. Priarone, Nucleate boiling and critical heat flux of HFE-7100 in horizontal narrow spaces, Exp. Therm. Fluid Sci. 35 (5) (2011) 772–779, http://dx.doi.org/10.1016/j.expthermflusci.2010.06.009, URL: https://www.sciencedirect.com/science/article/pii/S0894177710001214. 7th ECI-International Conference on Boiling Heat Transfer – ICBHT-2009.

[33] I.S. Kiyomura, J.M. Nunes, R.R. de Souza, S.S. Gajghate, E.M. Cardoso, Effect of microfin surfaces on boiling heat transfer using HFE-7100 as working fluid, J. Braz. Soc. Mech. Sci. Eng. 42 (7) (2020) 2366, http://dx.doi.org/10.1080/08916150390242244.

[34] E. dos Santos Filho, I.S. Kiyomura, B. Alves de Andrade, E.M. Cardoso, Pool boiling performance of HFE-7100 on hierarchically structured surfaces, Case Stud. Therm. Eng. 28 (2021) 101536, http://dx.doi.org/10.1016/j.csite.2021.101536, URL: https://www.sciencedirect.com/science/article/pii/S2214157X21006997.

[35] F. Wu, T. Hisano, Y. Umehara, Y. Takata, S. Mori, Improvement in the onset of the nucleate pool boiling of HFE-7100 with the use of a honeycomb porous plate and heated fine wire, Int. J. Heat Mass Transfer 217 (2023) 124738, http://dx.doi.org/10.1016/j.ijheatmasstransfer.2023.124738, URL: https://www.sciencedirect.com/science/article/pii/S0017931023008839.

[36] G. Mlakar, C.N. Huang, C. Kharangate, Effects of surface modifications on pool boiling heat transfer with HFE-7100, Int. J. Thermofluids 17 (2023) 100286, http://dx.doi.org/10.1016/j.ijft.2023.100286, URL: https://www.sciencedirect.com/science/article/pii/S2666202723000083.

[37] I.T. Martins, P. Fariñas Alvariño, L. Cabezas-Gómez, A new methodology for experimental analysis of single-cavity bubble's nucleation, growth and detachment in saturated HFE-7100, Exp. Therm. Fluid Sci. 159 (2024) 111272, http://dx.doi.org/10.1016/j.expthermflusci.2024.111272, URL: https://www.sciencedirect.com/science/article/pii/S0894177724001419.

[38] W.M. Rohsenow, A method of correlating heat-transfer data for surface boiling of liquids, Trans. Am. Soc. Mech. Eng. 74 (6) (1952) 969–975, http://dx.doi.org/10.1115/1.4015984.

[39] J.M.S. Jabardo, E.F. da Silva, G. Ribatski, S.F. de Barros, Evaluation of the rohsenow correlation through experimental pool boiling of halocarbon refrigerants on cylindrical surfaces, J. Braz. Soc. Mech. Sicences Eng. 6 (2) (2004) 218–230, http://dx.doi.org/10.1590/S1678-58782004000200015, URL: https://doi.org/10.1590/S1678-58782004000200015.

[40] G. Ribatski, J.M. Jabardo, Experimental study of nucleate boiling of halocarbon refrigerants on cylindrical surfaces, Int. J. Heat Mass Transfer 46 (23) (2003) 4439–4451, http://dx.doi.org/10.1016/S0017-9310(03)00252-7, URL: https://www.sciencedirect.com/science/article/pii/S0017931003002527.

[41] K. Stephan, M. Abdelsalam, Heat-transfer correlations for natural convection boiling, Int. J. Heat Mass Transfer 23 (1) (1980) 73–87, http://dx.doi.org/10.1016/0017-9310(80)90140-4, URL: https://www.sciencedirect.com/science/article/pii/0017931080901404.

[42] S.S. Kutateladze, On the transition to film boiling under natural convection, Kotloturbostroenie No. 3 (1948) 10.

[43] I. Mudawar, A.H. Howard, C.O. Gersey, An analytical model for near-saturated pool boiling critical heat flux on vertical surfaces, Int. J. Heat Mass Transfer 40 (10) (1997) 2327–2339, http://dx.doi.org/10.1016/S0017-9310(96)00298-0, URL: https://www.sciencedirect.com/science/article/pii/S0017931096002980.

[44] S.G. Kandlikar, A theoretical model to predict pool boiling CHF incorporating effects of contact angle and orientation, J. Heat Transf. 123 (6) (2001) 1071–1079, http://dx.doi.org/10.1115/1.1409265, URL: https://doi.org/10.1115/1.1409265.

[45] C.K. Guan, J.F. Klausner, R. Mei, A new mechanistic model for pool boiling CHF on horizontal surfaces, Int. J. Heat Mass Transfer 54 (17) (2011) 3960–3969, http://dx.doi.org/10.1016/j.ijheatmasstransfer.2011.04.029, URL: https://www.sciencedirect.com/science/article/pii/S0017931011002481.

[46] J. Kim, S. Jun, R. Laksnarain, S.M. You, Effect of surface roughness on pool boiling heat transfer at a heated surface having moderate wettability, Int. J. Heat Mass Transfer 101 (2016) 992–1002, http://dx.doi.org/10.1016/j.ijheatmasstransfer.2016.05.067, URL: https://www.sciencedirect.com/science/article/pii/S0017931015316732.

[47] V.V. Yagov, Is a crisis in pool boiling actually a hydrodynamic phenomenon? Int. J. Heat Mass Transfer 73 (2014) 265–273, http://dx.doi.org/10.1016/j.ijheatmasstransfer.2014.01.076, URL: https://www.sciencedirect.com/science/article/pii/S0017931014001173.

[48] V. Kozitskii, Heat transfer coefficients for boiling of n-butane on surfaces of various roughness, Chem. Pet. Eng. 8 (1) (1972) 23–24.

[49] J. Du, C. Zhao, H. Bo, A modified model for bubble growth rate and bubble departure diameter in nucleate pool boiling covering a wide range of pressures, Appl. Therm. Eng. 145 (2018) 407–415.

[50] T. Hibiki, M. Ishii, Active nucleation site density in boiling systems, Int. J. Heat Mass Transfer 46 (14) (2003) 2587–2601, http://dx.doi.org/10.1016/S0017-9310(03)00031-0, URL: https://www.sciencedirect.com/science/article/pii/S0017931003000310.

[51] R.J. Moffat, Describing the uncertainties in experimental results, Exp. Therm. Fluid Sci. 1 (1) (1988) 3–17, http://dx.doi.org/10.1016/0894-1777(88)90043-X, URL: https://www.sciencedirect.com/science/article/pii/089417778890043X.

[52] Y. Haramura, Y. Katto, A new hydrodynamic model of critical heat flux, applicable widely to both pool and forced convection boiling on submerged bodies in saturated liquids, Int. J. Heat Mass Transfer 26 (3) (1983) 389–399, http://dx.doi.org/10.1016/0017-9310(83)90043-1, URL: https://www.sciencedirect.com/science/article/pii/0017931083900431.